

Article

Age and Composition of Columbite-Tantalite Group Minerals in the Spodumene Pegmatite from the Chakabeishan Deposit, Northern Tibetan Plateau and Their Implications

Wenli Sun ^{1,2,3}, Zhidan Zhao ^{2,*}, Xuanxue Mo ², Chunjing Wei ¹, Guochen Dong ², Xiaowei Li ², Wanming Yuan ², Tao Wang ⁴, Shuang Yang ², Bingzhang Wang ⁴, Tong Pan ⁴, Jie Han ⁴, Hongliang Cao ⁴, Yan Tang ² and Liangliang Zhang ²

¹ MOE Key Laboratory of Orogenic Belts and Crustal Evolution, School of Earth and Space Sciences, Peking University, Beijing 100871, China

² State Key Laboratory of Geological Processes and Mineral Resources, School of Earth Science and Resources, China University of Geosciences, Beijing 100083, China

³ Gansu Industry Polytechnic College, Tianshui 741025, China

⁴ Bureau of Geological Exploration and Development of Qinghai Province, Xining 810012, China

* Correspondence: zdzhao@cugb.edu.cn; Tel.: +86-10-8232-1115

Abstract: The Chakabeishan (CKBS) deposit is the first pegmatite-type Li-Be deposit discovered in the eastern North Qaidam Tectonic Belt (NQTB) of Tibetan Plateau. The correct understanding of its petrogenesis and the precise determination of its formation age are of great significance for further regional prospecting and the discovery of new economically valuable rare-metal deposits. Therefore, a systematic study of texture, major-element composition, and U-Pb dating of columbite-tantalite group minerals (CGMs) in the spodumene pegmatite dyke from the CKBS deposit was undertaken. Three types of CGMs were identified, including concentric oscillatory ferrocolumbite (CGMs-1), homogeneous ferrocolumbite (CGMs-2), and irregular ferrotantalite (minor manganocolumbite) with abundant early ferrocolumbite replacement remnants (CGMs-3). The zoning patterns and chemical compositions in the CGMs record the complex evolutionary history of their host pegmatite from the magmatic stage (CGMs-1, disequilibrium crystallization) to the magmatic-hydrothermal transition stage (CGMs-2, equilibrium crystallization) and then to the late metasomatic stage (CGMs-3, replacement/re-equilibrium). CGMs U-Pb dating results suggest that the spodumene pegmatite dyke (No.15) emplaced at 230.1 ± 2.6 Ma. Subsequently, it experienced fluid metasomatism at 221 ± 5.3 Ma. Based on the new age data and published geochronological data, it can be concluded that the spodumene pegmatite dykes in the CKBS deposit formed in an oceanic subduction-related setting, representing a new metallogenic event in western China. Except for the CKBS deposit, a large number of rare-metal pegmatite dykes have also been discovered in the eastern NQTB, indicating that the eastern NQTB may be an important potential rare-metal metallogenic belt that should be explored in detail and arouse painstaking attention.

Keywords: CKBS deposit; CGMs; origin; U-Pb dating; a new belt



Citation: Sun, W.; Zhao, Z.; Mo, X.; Wei, C.; Dong, G.; Li, X.; Yuan, W.; Wang, T.; Yang, S.; Wang, B.; et al. Age and Composition of Columbite-Tantalite Group Minerals in the Spodumene Pegmatite from the Chakabeishan Deposit, Northern Tibetan Plateau and Their Implications. *Minerals* **2023**, *13*, 201. <https://doi.org/10.3390/min13020201>

Academic Editors: Callum Hetherington and Kunfeng Qiu

Received: 19 December 2022

Revised: 27 January 2023

Accepted: 28 January 2023

Published: 30 January 2023



Copyright: © 2023 by the authors. Licensee MDPI, Basel, Switzerland. This article is an open access article distributed under the terms and conditions of the Creative Commons Attribution (CC BY) license (<https://creativecommons.org/licenses/by/4.0/>).

1. Introduction

Rare metals (e.g., Li, Be, Nb, Ta, Rb and Cs) play a vital role in the modern electronic industry, medicine, new energy industry, national defense and other high-tech fields. No nation has all of the rare-metal resources it needs domestically, so international trade in rare metals is necessary [1]. If global supplies are considered to be at risk or insufficient to meet growing demand, international commerce may result in international competition for rare-metal resources. Against the background of competition for rare-metal resources, many countries have designated highly import-dependent rare metals as critical metals or strategic metals in the 21st century [1–3]. Granitic pegmatite (hereafter pegmatite) is one

of the important host rocks for rare metals, thus, it has attracted special attentions [4–9]. Pegmatite has been extensively documented over the last two centuries, but many fundamental problems remain unresolved, and new ones are coming to our attention, such as the role of hydrothermal process, the control factor for rare-metal mineralization and the geochemical fractionation of twin elements (e.g., Nb-Ta, Zr-Hf) [10–12]. One of the best ways to address the aforementioned issues is through textural and chemical variations in particular minerals, e.g., tourmaline [13,14], muscovite [15,16] and columbite-tantalite group minerals (CGMs) [17–19].

The Tibetan Plateau and its marginal areas contain a large number of rare-metal pegmatite dykes. The most fascinating region is the Tianshuihai-Songpan-Ganze terrane in the center of the Tibetan Plateau (Figure 1), where many super-large to medium-sized Li deposits, with a total Li_2O resource of >14.8 Mt, have been found [20–24]. These pegmatite-type Li deposits have close temporal, spatial, and genetic relationships to Triassic S-type granites and flysch sedimentary rocks; therefore, it is also called the Markam-Yajiang-Karakoram giant Li ore belt (MYKB), which formed in an orogenic setting in the Paleo-Tethys tectonic domain [20,24,25]. The eastern NQTB, located to the north of the MYKB, also developed significant Triassic granitoids associated with orogenic events in the Paleo-Tethys tectonic domain [21,26,27]. Recently, numerous pegmatite dykes and several pegmatite-type rare-metal deposits/mineralized points have been discovered in the eastern NQTB, including Honglingbei Li-Be mineralization point, Chakabeishan (CKBS) Li-Be deposit, Qiemoge Li-Be deposit, and so on [28–33]. The genetic relationship between pegmatite-type rare-metal deposits in the eastern NQTB and MYKB is less discussed. Whether they are products of the same magmatic-tectonic event is worth investigating, which is vital for regional rare-metal prospecting.

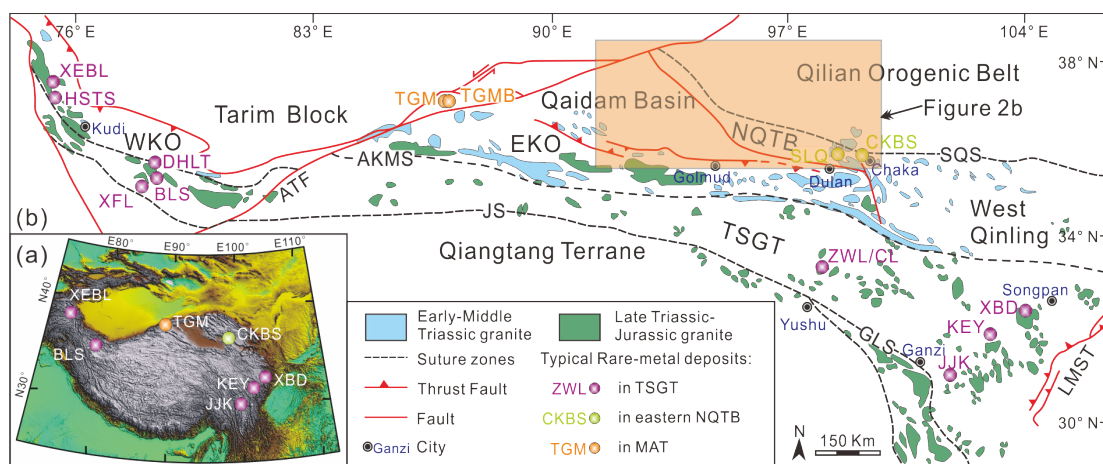


Figure 1. (a) Topographic map showing typical rare-metal deposits in the Tibetan Plateau. (b) Geological sketch showing the distributions of Late Triassic to Early Jurassic igneous rocks and major pegmatite-type rare-metal deposits in the NQTB and neighboring tectonic zones (modified after Yan et al. [20]; Liu et al. [21]). Abbreviations of tectonic units: TSGT = Tianshuihai-Songpan-Ganzi Terrane, EKO = Eastern Kunlun Orogen, WKO = Western Kunlun Orogen, MAT = Middle of Altyn Tagh. Abbreviations of geological boundaries: GLS = Ganzi-Litang suture, JS = Jinsha suture, AKMS = Ayimaqin-Kunlun-Matztagh suture, SQS = South Qilian suture, LMST = Longmenshan thrust, ATS = Altyn Tagh fault. Abbreviations of typical rare-metal deposits: BLS = Bailongshan, MLC = Mulinchang, XEBL = Xiaoerbulong, HSTS = Huoshitashi, XFL = Xuefengling, DHLT = Da-hongliutan, ZWL = Zhawulong, CL = Caolong, JJK = Jiajika, KEY = Ke’eryin, XBD = Xuebaoding, TGM = Tugman, TGM B = TugmanBei, CKBS = Chakabeishan and SLQ = Shaliuquan.

In this paper, we focus on the internal zoning pattern, major-element composition, and U-Pb isotope of CGMs (AB_2O_6 , A = Mn, Fe, B = Nb, Ta) in the spodumene-bearing pegmatite from the CKBS Li-Be deposit with the aim of revealing the evolutionary history of

the Li-rich pegmatite, determining the formation age of the host pegmatite, and deciphering the relationship between the CKBS deposit and rare-metal deposits in adjacent tectonic units. The results of this study can potentially aid in the exploration of new rare metal mineralization in the eastern section of the North Qaidam Tectonic Belt (NQTB).

2. Geological Backgrounds

The NQTB is situated on the northern margin of the Tibetan Plateau (Figure 2a), with the Qaidam Block to the south, the Qilian Block to the north, the Altyn Tagh fault to the west and the West Qinling Orogen to the east [33–37]. The NQTB is divided into a northern unit and a southern unit by the E-W-trending Yuka-Wulan fault (Figure 2b). The southern unit is an Early Paleozoic subduction-collision complex related to Proto-Tethys Ocean subduction. It is well known for ultra-high pressure (UHP) metamorphic rocks [37,38]. The northern unit, also known as Quanji Massif or Olongbuluke Massif, mainly consists of Proterozoic metamorphic basement and Phanerozoic sedimentary rocks [35,36,39]. More detailed information about the NQTB can be found in the work of Wang et al. [32], Chen et al. [34], Song et al. [38], Pan et al. [40], and Liu et al. [41].

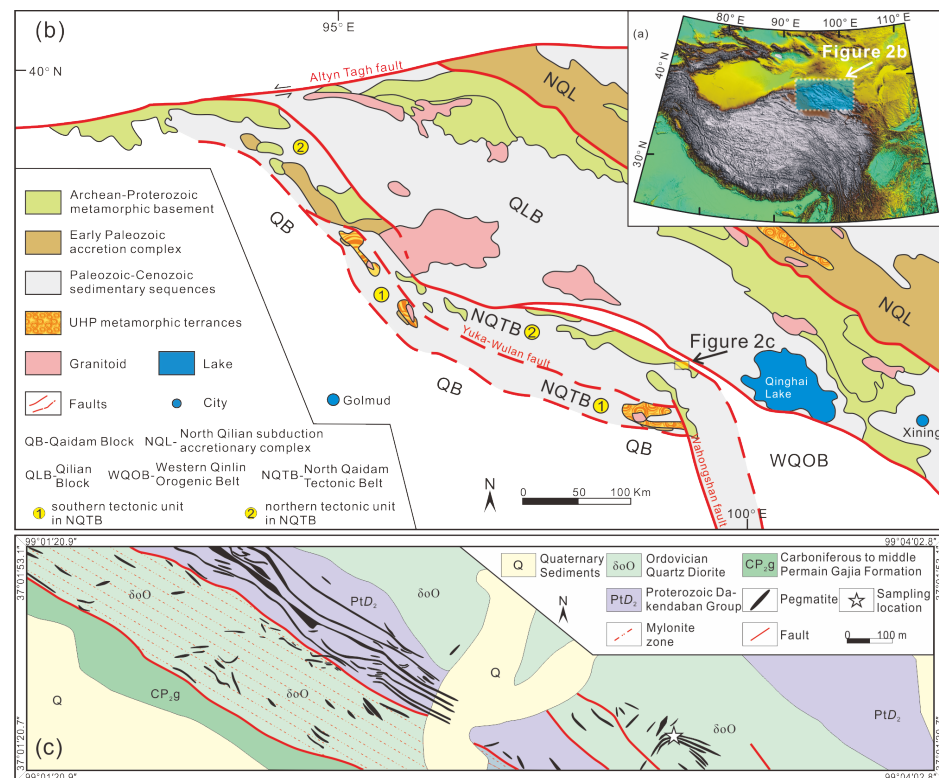


Figure 2. (a) Topographic map showing the location of (b); (b) Geological sketch of the NQTB and its surrounding tectonic units (modified after Chen et al. [34], Li et al. [35] and Ren et al. [36]); (c) Geological sketch showing the typical area of the CKBS Li-Be deposit and sampling location (modified after 1:10,000 geological survey data).

The CKBS deposit is the first pegmatite-type Li-Be deposit discovered in the eastern segment of NQTB (Figure 2b). There are *ca.* 800 LCT-type pegmatite dykes in the CKBS deposit, which were derived from high fractional crystallization of granitic magmas [42,43]. These pegmatite dykes occurred in the Paleoproterozoic Dakendaban Group schist Formation and the Ordovician quartz diorite (Figure 2c). The elongation of these pegmatites varies but generally shows NW-SE trending with varying dipping (23° – 83°). These pegmatite dykes are *ca.* 10–400 m in length and *ca.* 0.5–5 m in width. Since its first discovery in 2018, Li-Be resources of *ca.* 14,200 t Li_2O and *ca.* 7000 t BeO have been identified [31]. More detailed information on the pegmatites and ore-body in the CKBS deposit can be found in

the work of Liu et al. [21], Wang et al. [32], Pan et al. [40], and Liu et al. [41]. In the past four years, the formation ages of pegmatite dykes in this deposit, with greater controversy, have been suggested, including 240.6 ± 1.5 Ma [40] and 217–215 Ma [21] by coltan U-Pb dating; 213–211 Ma by muscovite Ar-Ar dating [21,44]; 216.6 ± 0.88 Ma by lepidolite Ar-Ar dating [21]; 235.9 ± 2.3 Ma and 217 ± 1.8 Ma by zircon U-Pb dating [32].

3. Samples

The investigated pegmatite samples were collected from the No.15 spodumene pegmatite dyke in the CKBS deposit, which is emplaced in the Ordovician diorite and mainly consists of spodumene, albite, feldspar, and quartz, with minor muscovite, tourmaline, and garnet (Figures 2c and 3). Although CGM grains were not directly observed within double polished thin sections and hand specimens, they were successfully separated from the investigated samples using conventional heavy liquid and magnetic methods and then hand-picked under a binocular microscope. The CGM grains were extracted, mounted in epoxy resin, and polished by standard methods. The images of back-scattered electron (BSE), transmitted light, and reflected light were obtained to ensure that the CGM grains are fresh and free of inclusions or cracks.

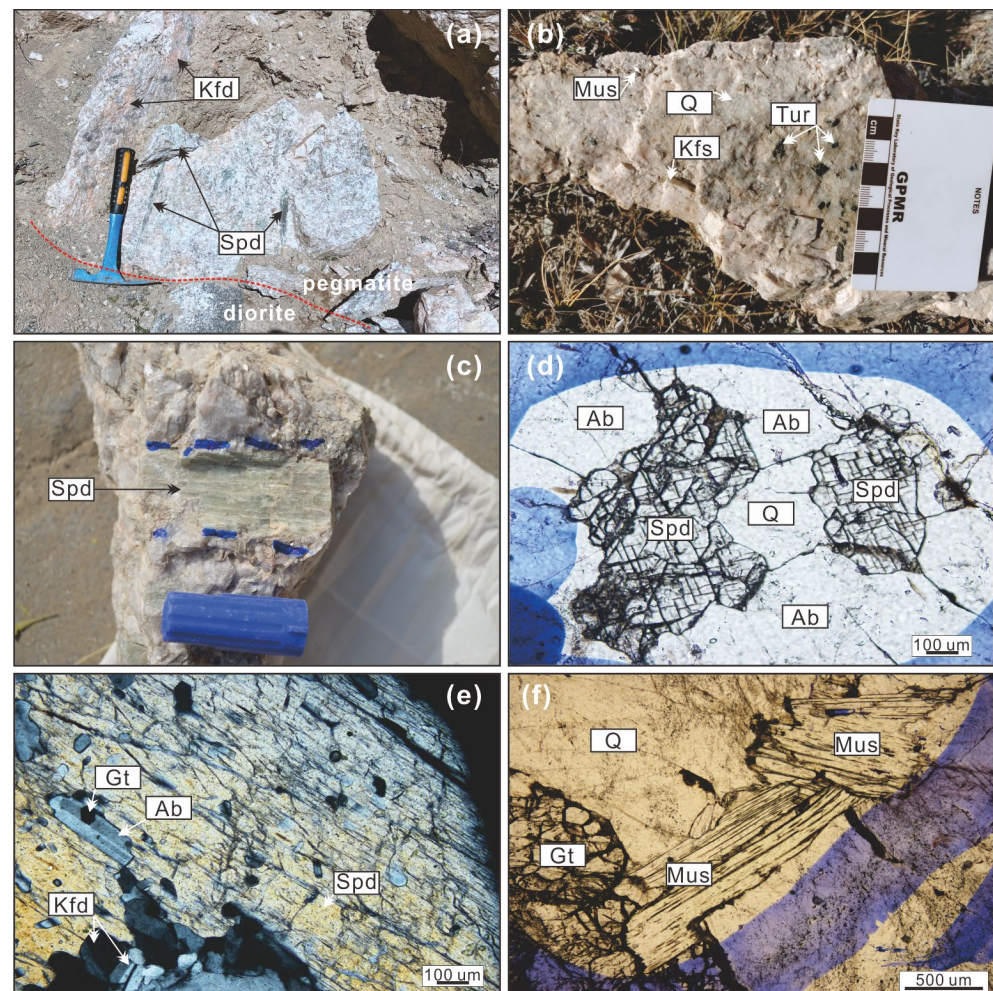


Figure 3. Photographs and photomicrographs showing mineral assemblages of the spodumene pegmatite dykes in the CKBS Li-Be deposit. (a) The pegmatite dyke intruded into diorite. (b) Hand-specimen of pegmatites in the CKBS deposit. (c) Photograph of a coarse green spodumene crystal. (d–f) Photomicrographs of the spodumene-bearing pegmatite on double polished thin sections. Spd—spodumene, Tur—tourmaline, Mus—muscovite, Ab—albite, Kfd—feldspar, Gt—garnet and Q—quartz.

As shown in Figure 4, the lengths and widths of the investigated CGM grains are *ca.* 100–350 μm and *ca.* 50–150 μm . Based on conspicuously different zoning patterns in the BSE images, three types of CGMs were identified: concentric oscillatory CGMs-1 (Figure 4a,b), homogeneous dark CGMs-2 (Figure 4c), and irregular patchy/complex CGMs-3 (Figure 4d–i). CGMs-3 grains are commonly composed of dark domains (CGMs-3a) and bright domains (CGMs-3b), showing obvious replacement phenomena, such as overgrowth, crosscutting, corrosion, and embayment (Figure 4d–i). CGMs-1 grains are rare, with only three in this study, whereas CGMs-2 and CGMs-3 particles are common.

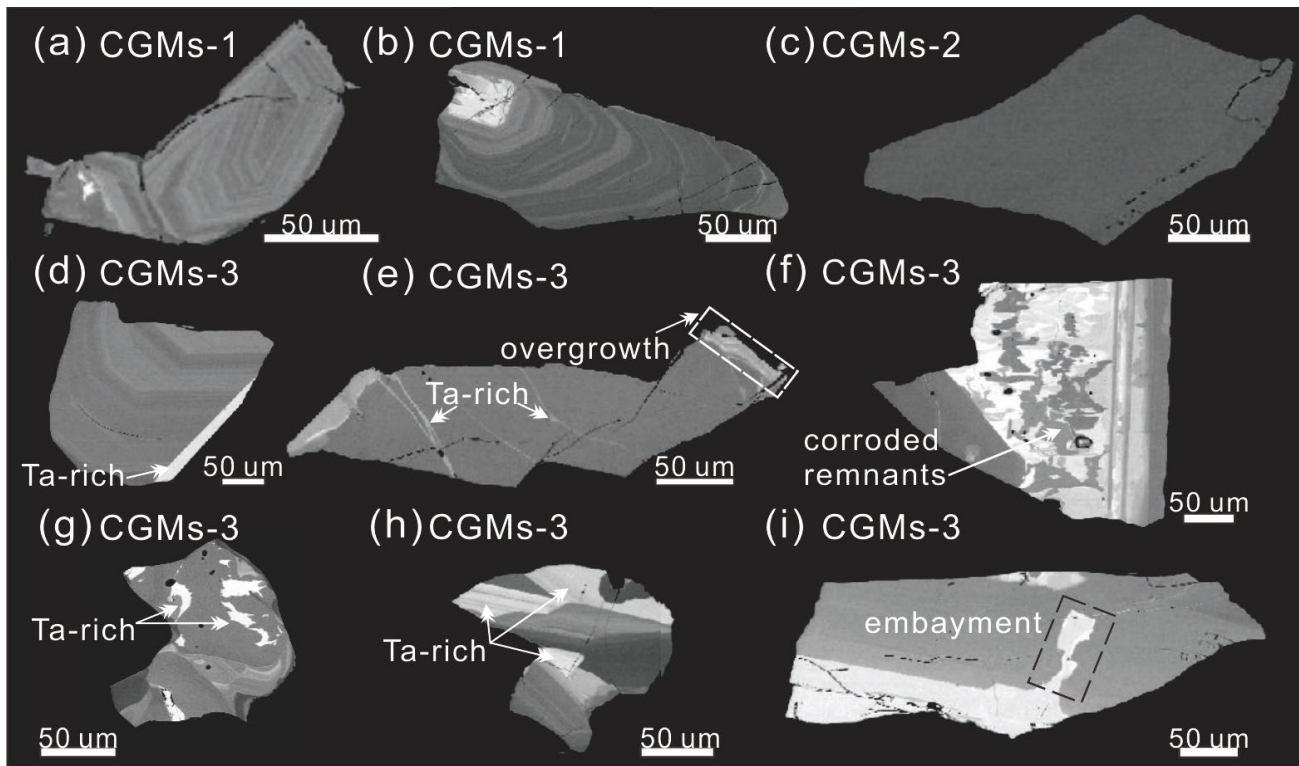


Figure 4. Back-scattered electron images of the CGMs. (a,b): oscillatory CGMs-1 grains; (c): homogeneous CGMs-2 crystal; (d): Ta-rich patch overgrowth on CGMs-1; (e): Ta-rich domains crosscutting Nb-rich domain; (f): corroded Nb-rich fragments remained in the Ta-rich domain (metasomatic relict texture); (g): small worm-like Ta-rich domains occurred into the Nb-rich domain (metasomatic myrmekitic texture); (h): CGMs-3 with mottled zoning; (i): CGMs-3 with embayment texture.

4. Analytical Methods

4.1. Major-Element Analyses

Major-element concentrations were analyzed by JEOL JXA8230 at Wuhan SampleSolution Analytical Technology Co., Ltd. (Wuhan, China), using a 20 kV accelerating voltage, 20 nA beam current, and 1 μm beam diameter. Peak and background counting times for all investigated elements were 10 s and 5 s, respectively. Data were corrected by the ZAF method provided by JEOL and the following standards were used: TiO_2 for Ti, $\text{CaMnSi}_2\text{O}_6$ for Ca, $\text{NaAlSi}_2\text{O}_6$ for Na, SnO_2 for Sn, MnSiO_3 for Mn, FeCr_2O_4 for Fe, Bi_2Se_3 for Bi, $\text{Mg}_3\text{Al}_2\text{Si}_3\text{O}_{12}$ for Al, PbS for Pb and pure metals for Ta, Nb, Pb, U and W. To reveal the chemical variations in the oscillatory zoning, EMPA mapping was performed on typical CGMs-1 grains using the JEOL JXA8230 at the same company, using a 20 kV voltage and 50 nA beam current. The dwell time is 50 ms, the image pixel lattice size is $1 \times 1 \mu\text{m}$, and the pixel size is 262×192 .

4.2. U-Pb Analyses

The in-situ U-Pb dating for CGMs grains was performed at the Mineral Laser Microprobe Analysis Laboratory, China University of Geosciences, Beijing (CUGB), China, using an Agilent 7900 Quadrupole Inductively Coupled Plasma Mass Spectrometry (Agilent, Santa Clara, CA, USA) coupled with an ASI RESOLUTION S115LR laser ablation system (Australian Scientific Instruments, Fyshwick, ACT, Australia). During the analyses, the laser spot size was 33 μm , energy density was 5 J/cm^2 , ablation time was 40 s, repetition rate was 5 Hz, and raster scanning speed was 5 $\mu\text{m}/\text{s}$. The dwell times for each mass scan were 10 ms for ^{232}Th , 15 ms for ^{238}U and ^{208}Pb , 20 ms for ^{204}Pb and ^{206}Pb , and 30 ms for ^{207}Pb . During analysis, Coltan 139 was used to correct the ratios of $^{206}\text{Pb}/^{238}\text{U}$, $^{207}\text{Pb}/^{235}\text{U}$ and $^{207}\text{Pb}/^{206}\text{Pb}$ (ID-TIMS age of 506 ± 2.3 Ma, [45]); NP-2 was used to monitor instrument status and experimental results. Offline data analysis and processing were undertaken with the Iolite software (Iolite Softwares Inc., Laurel, MD, USA). In addition, Isoplot v.4.15 software (Berkeley Geochronology Center, Berkeley, CA, USA) was used to plot Tera–Wasserburg diagrams and calculate weighted mean U-Pb ages [46].

5. Results

5.1. Major-Element Composition

All analysis results by EMPA are listed in Table S1. The abundance ranges, average values, and standard deviations of major element compositions in the CGMs are shown in Table 1. The results of EMPA mapping for CGMs-1 grains are shown in Figure 5. The three types of CGM show marked differences in chemical composition. Among, the CGMs-1 grains are characterized by episodic Nb- and Ta-rich zones alternating to each other (Figure 5), coupled with episodic concentrations of TiO_2 (0.290–0.439 wt.%), WO_3 (0.276–0.497 wt.%) and PbO (0.254–0.393 wt.%) (Figure 6a–c). The ratios of $\text{Ta}/(\text{Ta} + \text{Nb})$ and $\text{Mn}/(\text{Mn} + \text{Fe})$ in CGMs-1 range from 0.141–0.204 and 0.273–0.318, respectively. Compared with CGMs-1, CGMs-2 grains have slightly lower $\text{Ta}/(\text{Ta} + \text{Nb})$ ratios (0.069–0.120) and elevated $\text{Mn}/(\text{Mn} + \text{Fe})$ ratios (0.292–0.474). The ratios of $\text{Ta}/(\text{Ta} + \text{Nb})$ (0.058–0.168) and $\text{Mn}/(\text{Mn} + \text{Fe})$ (0.370–0.482) in CGMs-3a domains are comparable with those in CGMs-1 and CGMs-2. Compared with CGMs-3a domains, CGMs-3b domains display obviously increased Ta/Nb and slightly varied Mn/Fe , TiO_2 , SnO_2 , WO_3 , and PbO (Figure 6d–f).

Table 1. Major-element compositional variations of the three-type CGMs in the spodumene pegmatite from the CKBS deposit.

	CGMs-1		CGMs-2		CGMs-3a		CGMs-3b	
	min–max	a \pm sd						
Nb_2O_5 (wt.%)	55.63–61.70	58.92 \pm 1.862	63.66–69.27	67.75 \pm 1.413	58.34–70.41	66.11 \pm 4.455	20.66–59.87	40.80 \pm 12.79
Ta_2O_5 (wt.%)	16.78–23.73	19.81 \pm 2.071	8.496–14.47	9.924 \pm 1.380	7.187–19.56	11.76 \pm 4.431	17.11–62.22	38.99 \pm 14.27
TiO_2 (wt.%)	0.290–0.439	0.361 \pm 0.049	0.341–0.556	0.420 \pm 0.048	0.310–0.565	0.449 \pm 0.090	0.192–0.951	0.447 \pm 0.178
SnO_2 (wt.%)	0.000–0.142	0.066 \pm 0.057	0.000–0.270	0.081 \pm 0.080	0.016–0.304	0.129 \pm 0.086	0.000–1.182	0.237 \pm 0.254
MnO (wt.%)	5.356–6.351	6.075 \pm 0.318	5.980–9.698	8.148 \pm 0.987	7.376–9.518	8.224 \pm 0.679	6.163–11.89	7.849 \pm 1.395
FeO (wt.%)	13.51–14.44	13.84 \pm 0.293	10.91–14.72	12.52 \pm 1.031	10.34–13.24	12.21 \pm 0.973	7.121–13.74	10.38 \pm 1.729
WO_3 (wt.%)	0.276–0.497	0.383 \pm 0.067	0.261–0.575	0.388 \pm 0.078	0.278–0.511	0.408 \pm 0.079	0.215–1.608	0.398 \pm 0.253
PbO (wt.%)	0.254–0.393	0.319 \pm 0.046	0.174–0.427	0.363 \pm 0.048	0.275–0.426	0.337 \pm 0.047	0.000–0.343	0.188 \pm 0.093
Total (wt.%)	98.81–100.2	99.77 \pm 0.417	98.50–100.6	99.60 \pm 0.507	98.92–100.5	99.63 \pm 0.617	97.84–100.9	99.30 \pm 0.899
$\text{Mn}/(\text{Mn} + \text{Fe})$	0.273–0.318	0.308 \pm 0.015	0.292–0.474	0.397 \pm 0.049	0.370–0.482	0.406 \pm 0.039	0.312–0.628	0.435 \pm 0.075
$\text{Ta}/(\text{Ta} + \text{Nb})$	0.141–0.204	0.168 \pm 0.019	0.069–0.120	0.081 \pm 0.012	0.058–0.168	0.098 \pm 0.039	0.147–0.644	0.375 \pm 0.160

min–max: minimum value–maximum value; a: average value; sd: standard deviation; the numbers of analysis points for CGMs-1, CGMs-2, CGMs-3a and CGMs-3b are 12, 27, 9 and 30, respectively; details see Table S1.

As shown in Figure 7a, CGMs-1, CGMs-2, and CGMs-3a exclusively plot in the ferrocolumbite region, whereas the CGMs-3b domains are represented mainly by ferrocolumbite and ferrotantalite, and rarely by manganocolumbite. All CGMs show negative correlations in the diagrams of Nb (apfu) vs. Ta (apfu) and Mn (apfu) vs. Fe (apfu) (Figure 7b,c), suggesting the substitution of Ta with Nb and Fe with Mn in the three-type CGMs. The abundances of Nb, Ta, Fe, Mn, and Ti in the dark domains of CGMs-3 are comparable to those in CGMs-2 (Figure 7a–d). However, CGMs-3b show obviously different major element abundances from CGMs-1 and CGMs-2 (Figure 7a–d), especially Nb and Ta.

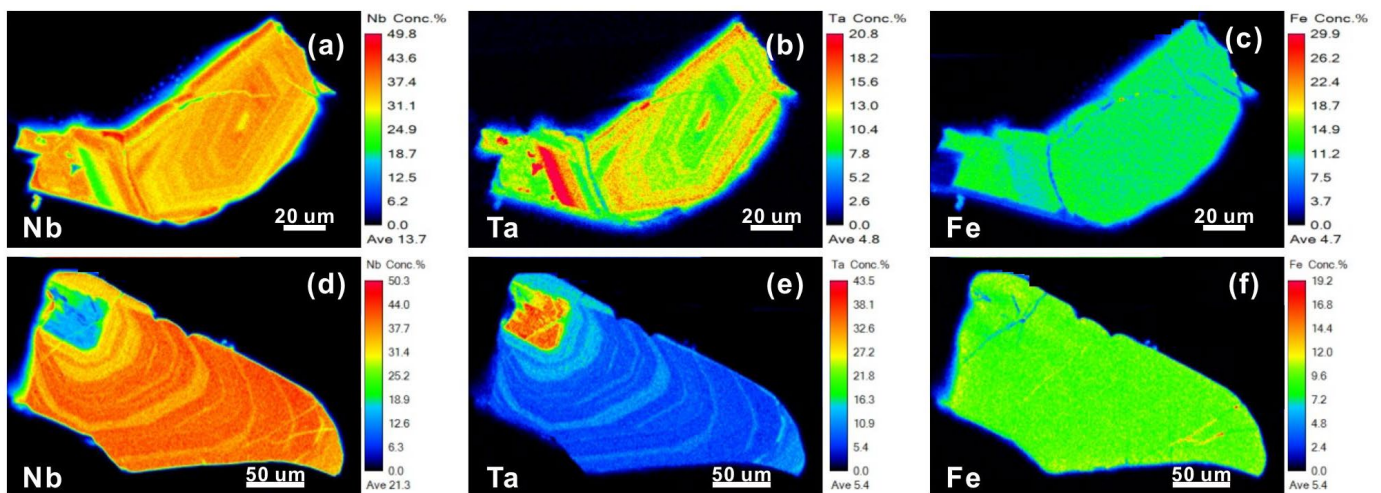


Figure 5. EMPA mapping for the oscillatory CGMs-1 grains. (a–c) for grain on Figure 4a and (d–f) for grain on Figure 4b.

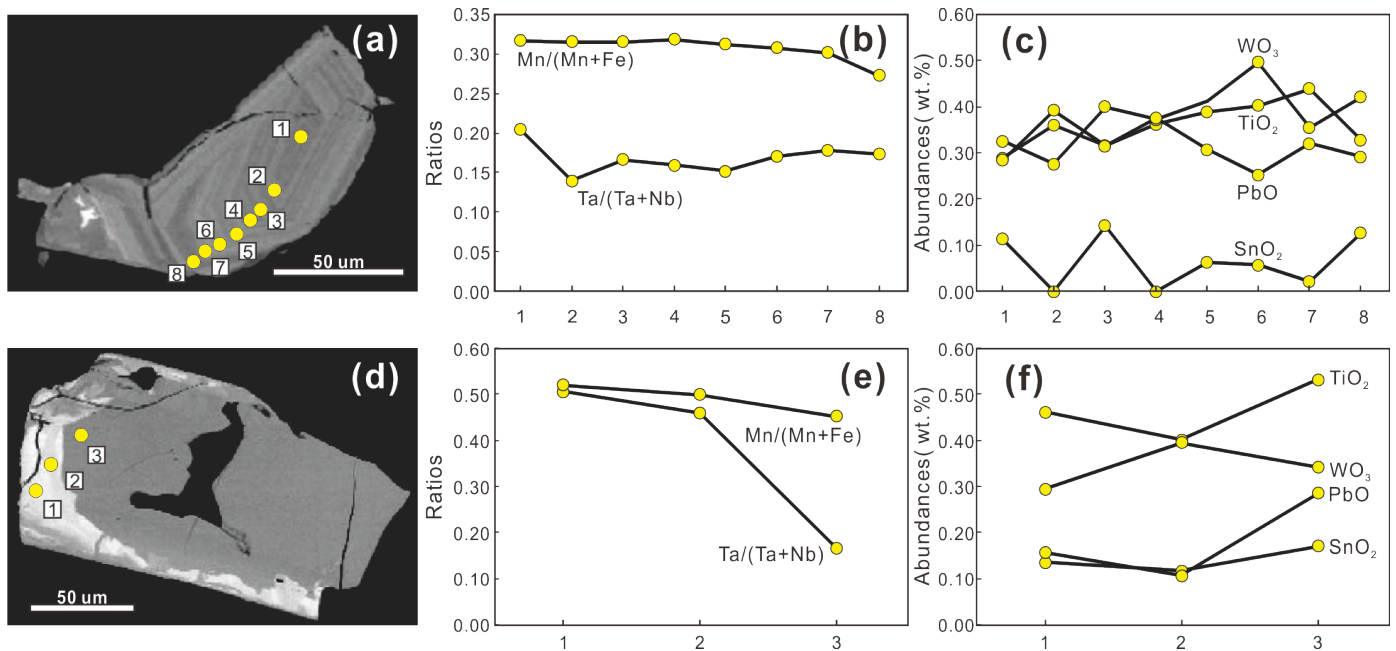


Figure 6. Electron probe microanalysis profiles showing the chemical variations of typical CGMs-1 (a–c) and CGMs-3 (d–f) from core to rim. Analyzed numbers and sites are marked as yellow circles (not to scale) in the backscattered electron images of (a,d), and the corresponding contents and ratios of elements are shown in the form of change curve (b,c,e,f).

5.2. U-Pb Ages

LA-ICP-MS U-Pb data for the CGMs are summarized in Table 2 and illustrated in Figure 8. Since there are few well-preserved CGMs-1 grains in the investigated pegmatite, we thus obtain only one analysis point with a $^{207}\text{Pb}/^{235}\text{U}$ ratio of 0.5570 and a $^{206}\text{Pb}/^{238}\text{U}$ ratio of 0.0398. The one point has a $^{206}\text{Pb}/^{238}\text{U}$ age of 252 ± 6.4 Ma. The ratios of $^{207}\text{Pb}/^{235}\text{U}$ and $^{206}\text{Pb}/^{238}\text{U}$ in CGMs-2 vary from 0.2490 to 0.4110 and 0.0364 to 0.0379, respectively. On the Tera–Wasserburg plot, the CGMs-2 grains are relatively scattered and yield an intercept age of 230.1 ± 2.6 Ma (2SD; MSWD = 1.3), with a weighted-mean $^{206}\text{Pb}/^{238}\text{U}$ age of 233.3 ± 3.5 Ma (2SD; MSWD = 2.6). The ratios of $^{207}\text{Pb}/^{235}\text{U}$ and $^{206}\text{Pb}/^{238}\text{U}$ in CGMs-3b vary from 0.236 to 0.262 and 0.0338 to 0.357, respectively. The seven CGMs-3b analyzed points yield an intercept age of 221.2 ± 5.3 Ma (2SD; MSWD = 2.8), with a

weighted-mean $^{206}\text{Pb}/^{238}\text{U}$ age of 220.8 ± 4.3 Ma (2SD; MSWD = 4.8). The intercept ages yielded by CGMs-2 and CGMs-3b agree well with their weighted-mean $^{206}\text{Pb}/^{238}\text{U}$ age.

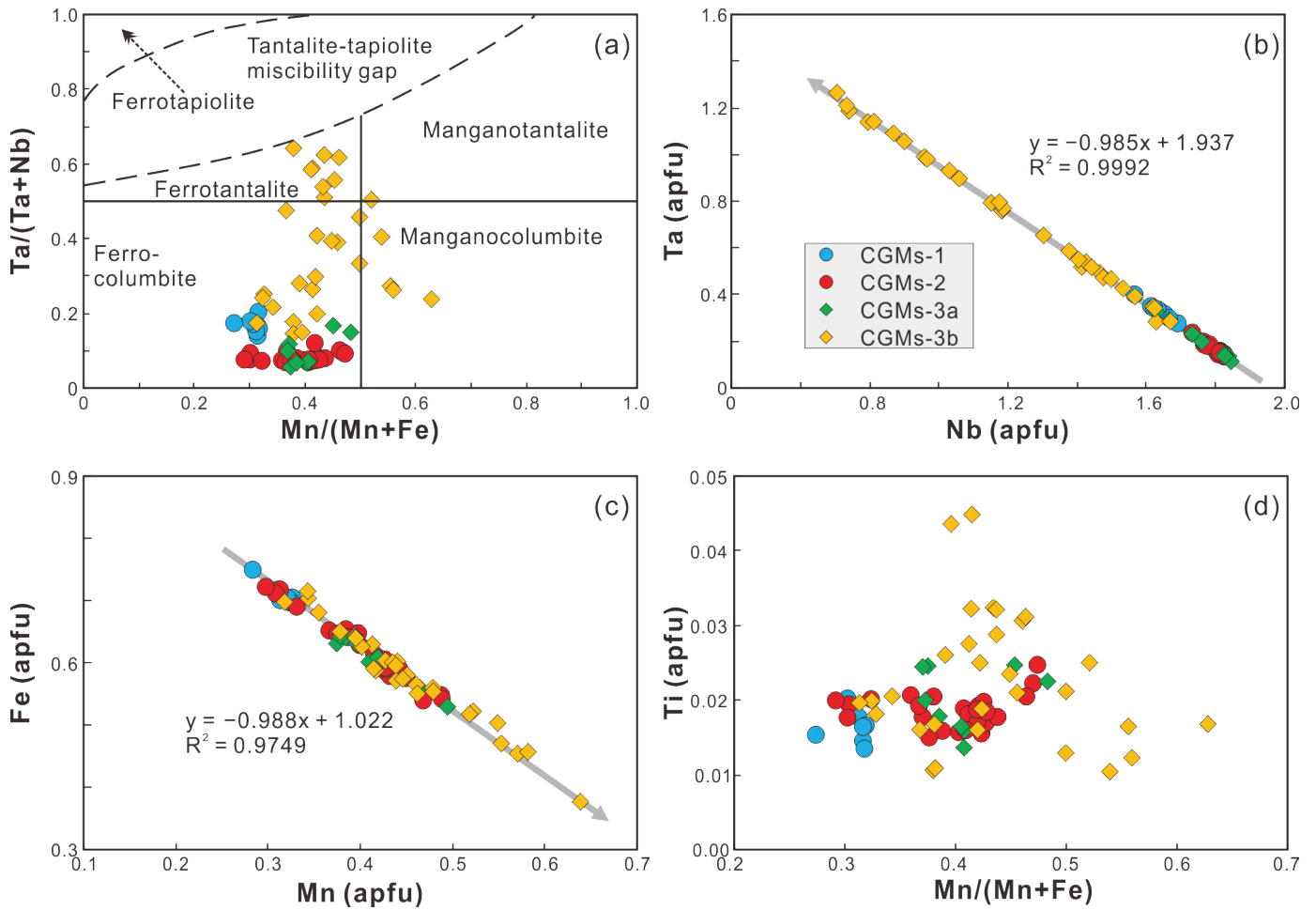


Figure 7. Major-element compositions in CGMs from the CKBS deposit expressed in terms of (a) Mn/(Mn + Fe) vs. Ta/(Ta + Nb) (after Černý and Ercit [17]), (b) Nb (apfu) vs. Ta (apfu), (c) Mn (apfu) vs. Fe (apfu) and (d) Mn/(Mn + Fe) vs. Ti (apfu).

Table 2. Analytical results of U-Pb isotopes and calculated ages for CGMs grains in the spodumene pegmatite from the CKBS deposit.

Spot No.	Type	Isotopic Ratios						Age (Ma)					
		$^{207}\text{Pb}/^{235}\text{U}$	2σ	$^{206}\text{Pb}/^{238}\text{U}$	2σ	$^{207}\text{Pb}/^{206}\text{Pb}$	2σ	$^{207}\text{Pb}/^{235}\text{U}$	2σ	$^{206}\text{Pb}/^{238}\text{U}$	2σ	$^{207}\text{Pb}/^{206}\text{Pb}$	2σ
1	CGMs-1	0.5570	0.0450	0.03980	0.00100	0.10010	0.00680	445	29	252	6.4	1570	130
2	CGMs-2	0.4100	0.0260	0.03760	0.00110	0.07810	0.00330	343	18	238	6.9	1062	89
3	CGMs-2	0.4110	0.0200	0.03714	0.00069	0.08010	0.00350	346	14	235	4.3	1114	92
4	CGMs-2	0.3160	0.0250	0.03643	0.00082	0.06110	0.00360	274	18	231	5.1	540	110
5	CGMs-2	0.2490	0.0130	0.03647	0.00068	0.04980	0.00260	224	11	231	4.2	150	110
6	CGMs-2	0.2780	0.0120	0.03640	0.00061	0.05610	0.00250	247	10	231	3.8	409	96
7	CGMs-2	0.3130	0.0260	0.03659	0.00087	0.06250	0.00530	273	20	232	5.4	500	170
8	CGMs-2	0.3840	0.0170	0.03792	0.00075	0.07380	0.00290	327	13	240	4.6	970	89
9	CGMs-3b	0.2420	0.0170	0.03569	0.00087	0.04990	0.00350	217	14	226	5.4	100	130
10	CGMs-3b	0.2370	0.0110	0.03412	0.00062	0.05100	0.00240	215	9	216	3.9	200	100
11	CGMs-3b	0.2490	0.0170	0.03573	0.00088	0.05200	0.00390	224	14	226	5.5	160	140
12	CGMs-3b	0.2470	0.0140	0.03453	0.00090	0.05200	0.00280	222	12	219	5.6	210	110
13	CGMs-3b	0.2360	0.0130	0.03375	0.00068	0.05150	0.00280	215	10	214	4.2	210	100
14	CGMs-3b	0.2620	0.0110	0.03520	0.00057	0.05370	0.00220	235	9	223	3.5	302	87
15	CGMs-3b	0.2435	0.0075	0.03529	0.00056	0.04980	0.00150	221	6	224	3.5	162	65

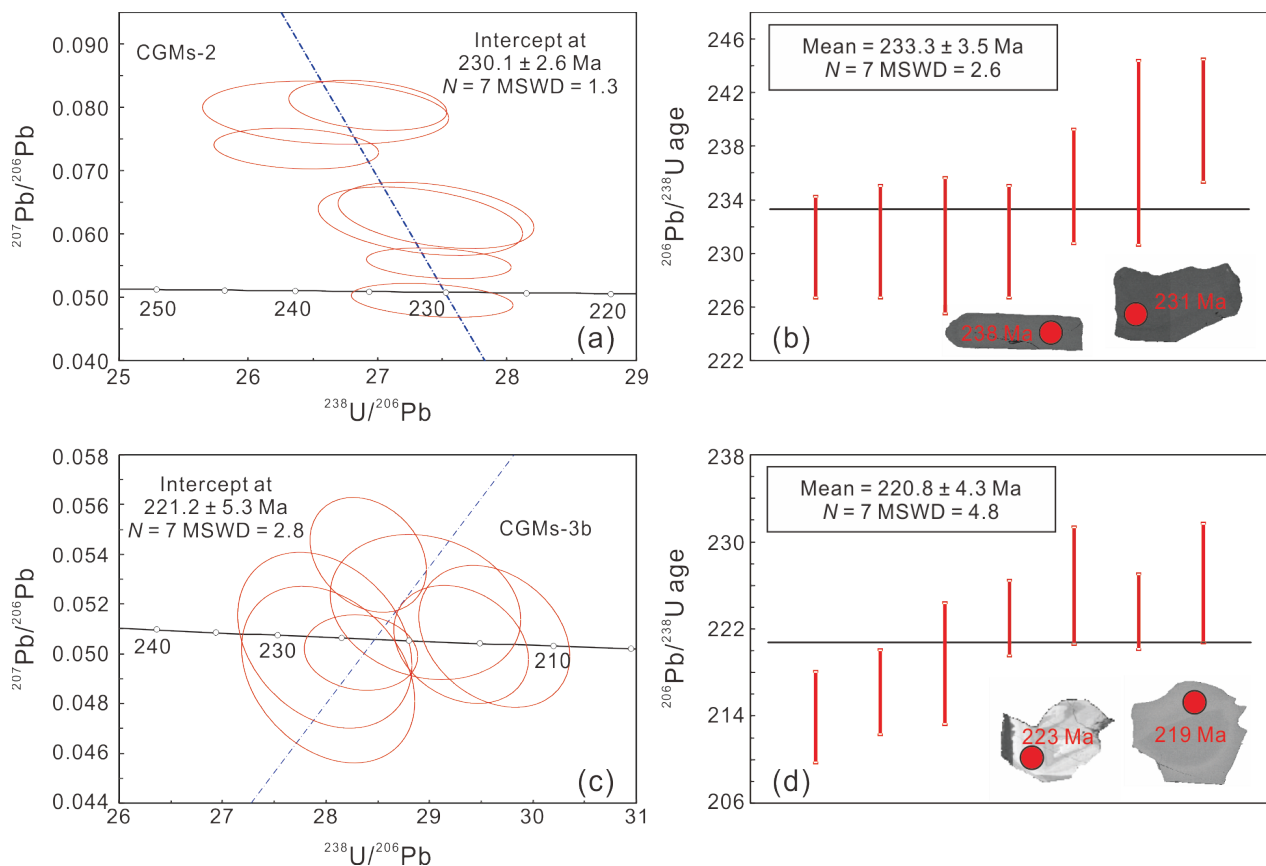


Figure 8. Tera-Wasserburg (a) and weighted average (b) diagrams for CGMs-2. Tera-Wasserburg (c) and weighted average (d) diagrams for CGMs-3b. Red circles and red words on the BSE images of typical CGM crystals showing U-Pb analyzed sites and results ($^{206}\text{Pb}/^{238}\text{U}$ ages), respectively.

6. Discussions

6.1. CGMs Origin and Chemical Evolution

Both primary magmatic and secondary metasomatic models have been suggested for the genesis of CGMs in the hydrous granitic magma systems. The magmatic origin of CGMs has been established by both experimental determinations and natural samples [47–50]. The researchers favoring a magmatic model suggested that the CGMs commonly coexist with other rock-forming minerals, show simple textures (oscillatory zoning, homogeneous, progressive normal/reverse zoning), and display gradual or periodical variations in Ta/(Ta + Nb) and/or Mn/(Mn + Fe) from core to rim [49–55]. The main pieces of evidence cited for a metasomatic model are that the CGMs show patchy/complex textures with two distinctly different chemical domains (mainly expressed in the ratios Ta/Nb and Mn/Fe), and coexist with secondary minerals (e.g., wadginite, microlite), and occur in replacement bodies [19,40,48,49,54]. It is worth noting that a recent experimental study suggested that homogenous CGMs with magmatic textures could crystallize from fluid–melt interactions in a hydrous granitic system, where CGMs saturations are reached at geologically reasonable concentrations of high field strength elements (HFSE, e.g., Nb, Ta) in melts and fluid-mobile elements (FME, e.g., Mn, Fe) in hydrothermal fluids [50]. The experiment demonstrated that CGMs can form at the magmatic-hydrothermal stage and require two-end members, rather than always resulting from a single melt or fluid phase as previously reported. The question arises as to whether the CGM grains in the spodumene pegmatite from the CKBS deposit were formed through magmatic processes, metasomatic processes, or fluid–melt interactions.

6.1.1. Primary CGMs-1 and CGMs-2

The oscillatory zoning in the CGMs-1 ferrocolumbite is concentric and continuous, which is different from the irregular, discontinuous oscillatory zoning in metasomatic CGMs [56], indicating that CGMs-1 are of non-metasomatic origin. The textural pattern in CGMs-1 is similar to that in magmatic CGMs from granite and pegmatite worldwide, such as Shangbao granite [47], Ineigi granite [48], Penouta leucogranite [52], Separation Lake pegmatite [19], Tanco Lower pegmatite [49], Jezuitské Lesy pegmatite [57], and Koktokay No.3 pegmatite [5], implying that CGMs-1 have a syn-magmatic origin. The magmatic origin of the CGMs-1 is further supported by the coupled chemical oscillatory zoning, including periodical variations in the concentrations of Ta, Nb, Ti, Sn, W and Pb (Figures 5 and 6c). The chemical oscillatory zoning in magmatic CGMs from pegmatites is believed to result from non-equilibrium fractional crystallization due to the slow diffusion of Nb and Ta, as well as Ti, Sn, W, and Pb, relative to the rate of crystal growth in the crystallization front of the pegmatite [49,56,58,59], which is described as a process of constitutional zone refining by London et al. [4].

Unlike CGMs-1, CGMs-2 ferrocolumbite grains are homogeneous in the BSE images (Figure 4c). The unzoned textural pattern in the CGMs-2 ferrocolumbite reflects balanced contributions of the main components [49,60,61], chiefly Nb and Ta (Figure 7a). This indicates that the CGMs-2 ferrocolumbite grains were products of equilibrium crystallization, which is significantly distinct from the non-equilibrium crystallization crystals of CGMs-1 ferrocolumbite. In the context of pegmatite, equilibrium-crystallization could take place in the condition of a silicate melt phase coexisting with an independent fluid phase [62,63], where CGMs might directly crystallize from the melt phase, or from the fluid phase, or form via melt-fluid interactions. The chemical and B-isotopic compositions in tourmaline indicated that Na-Fe-B-rich fluid exsolution occurred during the evolution of spodumene pegmatite from the CKBS deposit [43]. The Na-Fe-B-rich fluid cannot transport significant amounts of Nb and Ta to precipitate CGMs-2 ferrocolumbite directly, since melt-aqueous fluid partition coefficients for Ta and Nb are extremely low in the hydrous granitic melt system [12,64–66]. The solubility of Nb and Ta could be enhanced in fluoride solutions, mainly as HF [55,67,68]. However, we have to discount a major role of such fluid on the formation of CGMs-2, since F-rich minerals (e.g., lepidolite, fluorapatite, fluorite, topaz) are either scarce or absent in the investigated pegmatite (No.15), suggesting a low-F system rather than an F-rich one [69,70]. Furthermore, if CGMs-2 had crystallized directly from an F-rich fluid phase, they should have plotted in the Mn-rich region [19,69] rather than the Fe-rich region (Figure 7a). Unlike Nb and Ta, abundant Fe (a fluid mobile element, [60]) was incorporated into the Na-Fe-B-rich fluid phase during fluid-melt immiscibility, resulting in the residual melt phase hardly crystallizing ferrocolumbite directly due to the absence of bivalent cations. Thus, the most possible mechanism for the formation of homogeneous CGMs-2 ferrocolumbite grains is fluid-melt interactions, i.e., they formed via interactions of a melt that is enriched in HFSE (e.g., Nb, Ta) with a diffused fluid enriched in FME (e.g., Mn, Fe). The elevated Mn/(Mn + Fe) trend in the CGMs-2 ferrocolumbite crystals could be ascribed to the competitive crystallization of paragenetic Fe-rich minerals (e.g., hydrothermal tourmaline, [43]).

6.1.2. Secondary CGMs-3

The textures, such as corrosion, crosscutting, embayment, and overgrowth (Figure 4d–i), exclusively indicate the partial decomposition of CGMs-3a by later fluids/melts and the generation of a more Ta-rich CGMs-3b along with the margins and micro-cracks of crystals [19,49,58]. Since the CGMs-3a domains are comparable to CGMs-1 and CGMs-2 in texture patterns and chemical compositions (Figures 4 and 7), it is thus reasonable to infer that CGMs-3a are pristine domains of CGMs-1 and CGMs-2 remaining after alterations of CGMs-3b. The texture patterns in CGMs-3 are comparable to those in CGMs from hydrous granitic melts worldwide, such as Shihuiyao granite [61], Abu Dabbab granite [71], Big Whopper pegmatite [19], Kamativi pegmatite [69], Presqueira pegmatite [70], Mu-

fushan pegmatite [72], and Nanyangshan pegmatite [73], which was suggested to be of later fluid-induced or melt-induced replacement origin. If melt-induced model (Ta-rich melt replaced) were applied to CGMs-3, highly evolved injected melt could react with early crystallized rock-forming minerals and form replacement phenomena (e.g., muscovite replacement, [49]). However, replacement phenomena are not observed in the investigated spodumene pegmatite where all main rock-forming minerals boundaries are sharp (Figure 3). Thus, the most possible metasomatic medium for CGMs-3 was a special fluid phase, which might be regional metamorphic [74] or exsolved from the more evolved melt in the very last stages of fractionation [5,19,56,70]. There is no evidence for the pegmatite formation being connected to regional metamorphism either at the outcrop or thin section scale, suggesting the CGMs-3 recorded the variable conditions within the pegmatite-forming melt itself. This is further supported by the extremely wide range of composition in CGMs-3 expressed as ferrocolumbite, ferrotantalite and manganocolumbite (Figure 6a), since metamorphic fluid could homogenize the composition of CGMs whereas magmatic hydrothermal alteration results in diversification of the mineralogy of Nb and Ta [74]. Accordingly, it can be concluded that the special fluid for CGMs-3 formation was magmatic fluid that exsolved from the pegmatite-forming melt at the end of magmatic crystallization. Unfortunately, the available data in the study and reliable data in the associated papers are insufficient to constrain the physicochemical properties of the special fluid, warranting further work on this topic, especially fluid inclusions. As several case studies have shown [47,73], we suggest that the Ta-rich special fluids may be similar to hydrosilicate fluids that were rich in both H₂O and SiO₂ and had the capacity to dissolve Ta that accumulated in the terminal melts at temperatures ranging from 600 °C to relatively lower temperatures. It is worth noting that the special fluid phase is not the same fluid phase related to CGMs-2 formation in terms of textural relationships between CGMs-2 and CGMs-3, i.e., two fluid exsolution events occurred. By studying fluid inclusions, Alfonso and Melgarejo [75] have confirmed that fluid pulse exsolution could occur during the evolution of rare-metal pegmatite.

According to the study of the internal zoning patterns and element compositions, the formation process of CGMs and the evolution of the spodumene pegmatite are specifically reconstructed as follows (Figure 9): after the pegmatitic melt was emplaced into the shallow crust, Nb was initially saturated and primary CGMs-1 crystals with oscillatory zonation were crystallized directly from the melt in disequilibrium conditions. Subsequently, during the magmatic-hydrothermal transition stage, the homogeneous CGMs-2 crystals were generated via interactions of the evolved melt (enriched in Nb and Ta) with the diffused fluid (enriched in Fe and Mn). Finally, a special magmatic Ta-rich fluid (hydrosilicate?) exsolved from the imminently exhausted melt and led to the formation of secondary CGMs-3 grains by substituting the early formed CGMs-1 and CGMs-2.

6.2. Geochronological Framework and Implications

6.2.1. Previous Geochronology Review

Zircon U-Pb data revealed that spodumene pegmatite dykes in the CKBS deposit were emplaced at *ca.* 217 Ma [32]. However, these zircons experienced obvious metamictization and metasomatism, indicating that their U-Pb ages cannot represent the crystallization time of the host pegmatite [76]. The uncertainty of zircon U-Pb age in pegmatite-system has been demonstrated in many case studies, e.g., [21,76]. CGMs grains are regarded as an excellent U-Pb dating alternative for pegmatite-system due to their high U and low common Pb contents [24,45]. Pan et al. [40] were the first to report CGMs U-Pb age for spodumene pegmatite dykes in the CKBS deposit, where eleven homogenous dark CGMs grains yielded a weighted mean ²⁰⁶Pb/²³⁸U age of 240.6 ± 1.5 Ma. The textural patterns in the CGMs grains documented by Pan et al. [40] are comparable with those in CGMs-2, indicating that they formed at the magmatic-hydrothermal stage and their U-Pb ages could represent consolidation ages of the host pegmatite. Recently, Liu et al. [21] reported obviously younger CGMs U-Pb ages (217–215 Ma) for spodumene pegmatite dykes in

the CKBS deposit. After careful comparisons, it can be found that these CGMs grains of 217–215 Ma commonly show bright BSE images (Ta-rich domains), which are similar to the CGMs-3b domains in this study and the CGM grain of 211 Ma documented by Pan et al. [40], indicating they are of metasomatic origin and their U-Pb ages represent the time of late metasomatic events. This is further supported by the fact that the U-Pb ages of CGMs with bright BSE images (217–215 Ma) are comparable with muscovite Ar-Ar ages (217–212 Ma) and lepidolite Ar-Ar ages (*ca.* 217 Ma) [21,44], since the Ar-Ar isotopic systems in the muscovite/lepidolite are susceptible to being reset by late metasomatic events related to CGMs-3 formation due to the low closure temperature (350–400 °C, Burtt and Phillips [77]).

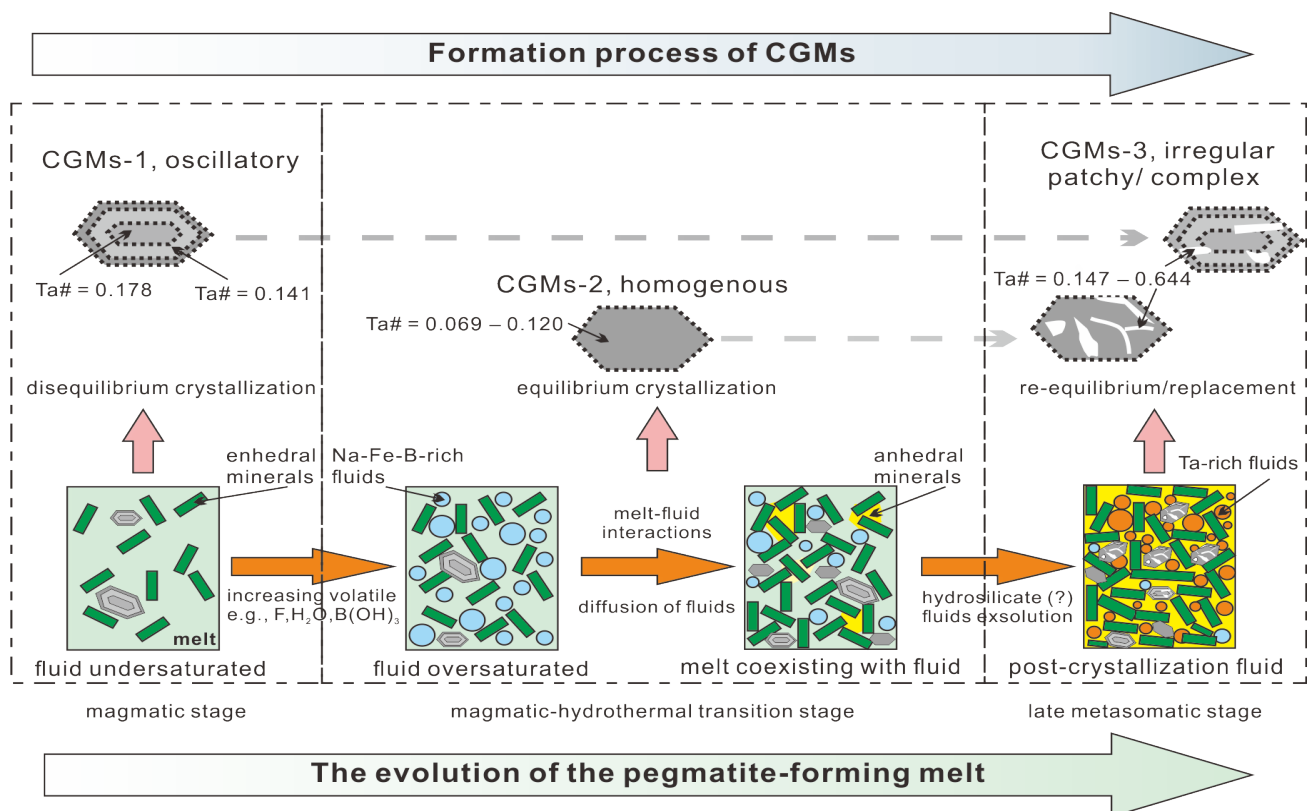


Figure 9. Schematic model illustrating the formation process of CGMs and the evolution of pegmatite. $Ta\# = Ta/(Ta + Nb)$. Note that the sizes of minerals are not to scale.

6.2.2. Geochronological Framework

In terms of the origin and evolution model for the CGMs crystals as discussed above, it would be accepted that the U-Pb ages of CGMs-1 and CGMs-2 represent the crystallization time of the host pegmatite whereas the secondary CGMs-3 U-Pb age is representative of late metasomatic time. One data point obtained for CGMs-1 has no apparent statistical significance, and its $^{206}\text{Pb}/^{238}\text{U}$ age of 252 ± 6.4 Ma hardly represents the crystallized age of host spodumene pegmatite. Because the cooling rate of pegmatite-forming melts after emplacement is rapid [4,78], it is reasonable to ignore the CGMs-1 U-Pb data and use the CGMs-2 intercept age as the crystallization time of the host pegmatite. Accordingly, we reconstruct the geochronological framework for the spodumene pegmatite dyke (No.15) in the CKBS deposit: a Li-B-rich pegmatite-forming melt phase was emplaced into the eastern NQTB and started to crystallize CGMs-1 and CGMs-2 at 230 ± 2.6 Ma. Subsequently, CGMs-1 and CGMs-2 grains were replaced to form CGMs-3 by a special fluid phase at 221 ± 5.3 Ma. Please note that the U-Pb ages of the primary and secondary CGMs are consistent within errors (minimum gap is *ca.* 1 Ma).

Comparing the new U-Pb data (Table 2, Figure 8) with published geochronological data [21,32,40,44], it can be concluded that the crystallization ages of the spodumene pegmatite dykes in the CKBS deposit are different, with a discrepancy of *ca.* 6–15 Ma within errors. As the consolidation of an individual pegmatite dyke should be finished in a short time [4,78], the age discrepancy of *ca.* 6–15 Ma reflects that (i) the Li-rich pegmatites in the CKBS deposit are not a cogenetic pegmatite group (defined by Černý [79]) although they are spatially close together, i.e., they might be derived from different sources, as documented in the pegmatites of the Fregeneda area [80] and the Kamativi area [69]; (ii) the pulse emplacements rather than a single emplacement of Li-rich pegmatite-forming melts in the CKBS deposit, i.e., multiple batches of Li-rich pegmatitic melts were emplaced into the shallow crust during a period of *ca.* 6–15 Ma. The latter scenario is difficult to reconcile with geological observations that a granitic magma chamber must be large enough to survive over *ca.* 6 Ma (1200 km² for *ca.* 10 Ma, [81]). So far, no contemporaneous S-type granite with such a large volume has been found around the CKBS deposit. The scenario of the pegmatites not being a cogenetic pegmatite group is more likely, which is supported by the numerous independent 255–235 Ma granitoids exposed around the CKBS deposit [21,42].

6.2.3. Tectonic Environment

Extensive Early-Middle Triassic arc igneous plutons are exposed near the studied area in the eastern NQTB, including the Wulan gabbro (245–242 Ma), the Tianjunnanshan granites (246 Ma), the Qinghaihunanshan granite (238 Ma), the Xugeigou granite (254 Ma), the Qiluoshan granodiorite (251 Ma), the Chahannuo hornblende diorite (249 Ma), the Chahannuo granite (248 Ma), the Chahanuo granodiorite (243 Ma), the Chahanhe granite (240 Ma), the Shailekeguolei granodiorite (249 Ma), and the Narong granitic porphyry (245 Ma) [21,27,40]. The formation ages and Nd-Hf isotopic compositions of these arc igneous plutons in the eastern NQTB are comparable to those of arc igneous rocks in the Buerhanbuda area (250–238 Ma) in the East Kunlun and the Tongren-Zeku area (242–234 Ma) in the West Qinling, indicating that the eastern NQTB, East Kunlun, and West Qinling were a complete active continental margin system during the Early-Middle Triassic, which was related to the northward subduction of the Paleo-Tethys oceanic plate [21,26]. Post-collision A-type granite plutons in the eastern NQTB (220–215 Ma) and East Kunlun (228–218 Ma) indicate that the Paleo-Tethys Ocean was closed in the Late Triassic [21]. Therefore, it would be accepted that the Middle Triassic pegmatites and adjacent Early-Middle Triassic granitoids in and around the CKBS deposit were formed in an oceanic subduction-related setting. The conclusion is consistent with Boroujerd pegmatites [82].

6.3. Regional Mineralization Comparison

Regionally, there are three important rare-metal metallogenic belts related to Tethys evolution around the CKBS deposit in the eastern NQTB (Figure 10a), including the world-class MYKB [21,24], the Guanpo-Danfeng mineralization belt (GDMB) [73,83,84] and the Tugman-Tashisayi mineralization belt (TTMB) [76,85]. The CKBS Li-Be deposit in the eastern NQTB and the pegmatite-type rare-metal deposits in the MYKB, GDTB and TGMB are products of extreme fractionation of peraluminous granitic intrusions [21,25,42,83,85,86]. Therefore, whether the CKBS deposit can be connected with one of the spatially adjacent MYKB, GDTB, and TTMB remains an interesting question, which is of great significance for regional prospecting. The following three reasons support the conclusion that the CKBS deposit is not connectible to the three spatially adjacent rare-metal mineralization belts. First, the formation ages of rare-metal deposits in the MYKB, GDMB, and TTMB are 224–144 Ma, 420–394 Ma, and 468–350 Ma, respectively, which are different from the crystallization age of the CKBS deposit (*ca.* 240–230 Ma, Table 3, Figure 10b–d). However, it is interesting to note that the late metasomatic ages of pegmatite dykes in the CKBS deposit overlap with the crystallization ages of some deposits in the MYKB (Figure 10d). Second, regionally comprehensive studies showed that the geological environments were late/post-orogenic regimes when rare-metal deposits formed in the MYKB, GDMB, and

TTMB [25,73,83,85], whereas the dynamic environment for the formation of spodumene pegmatite in the CKBS deposit was an active continental margin, indicating that they were controlled by different geological events. Third, Hf isotopic compositions in zircons are believed to be unaffected during metamictization, which thus could trace the source of host granitic rock [86]. The $\epsilon_{\text{Hf}}(t)$ values in zircons from the CKBS deposit varied from -15.5 to -11.63 [32] while those from the rare-metal deposits in the MYKB and GDMB ranged from -13.6 to -7.23 [86,87] and from -7.8 to -7.0 [83], respectively, indicating that the sources of these pegmatite-granite are different.

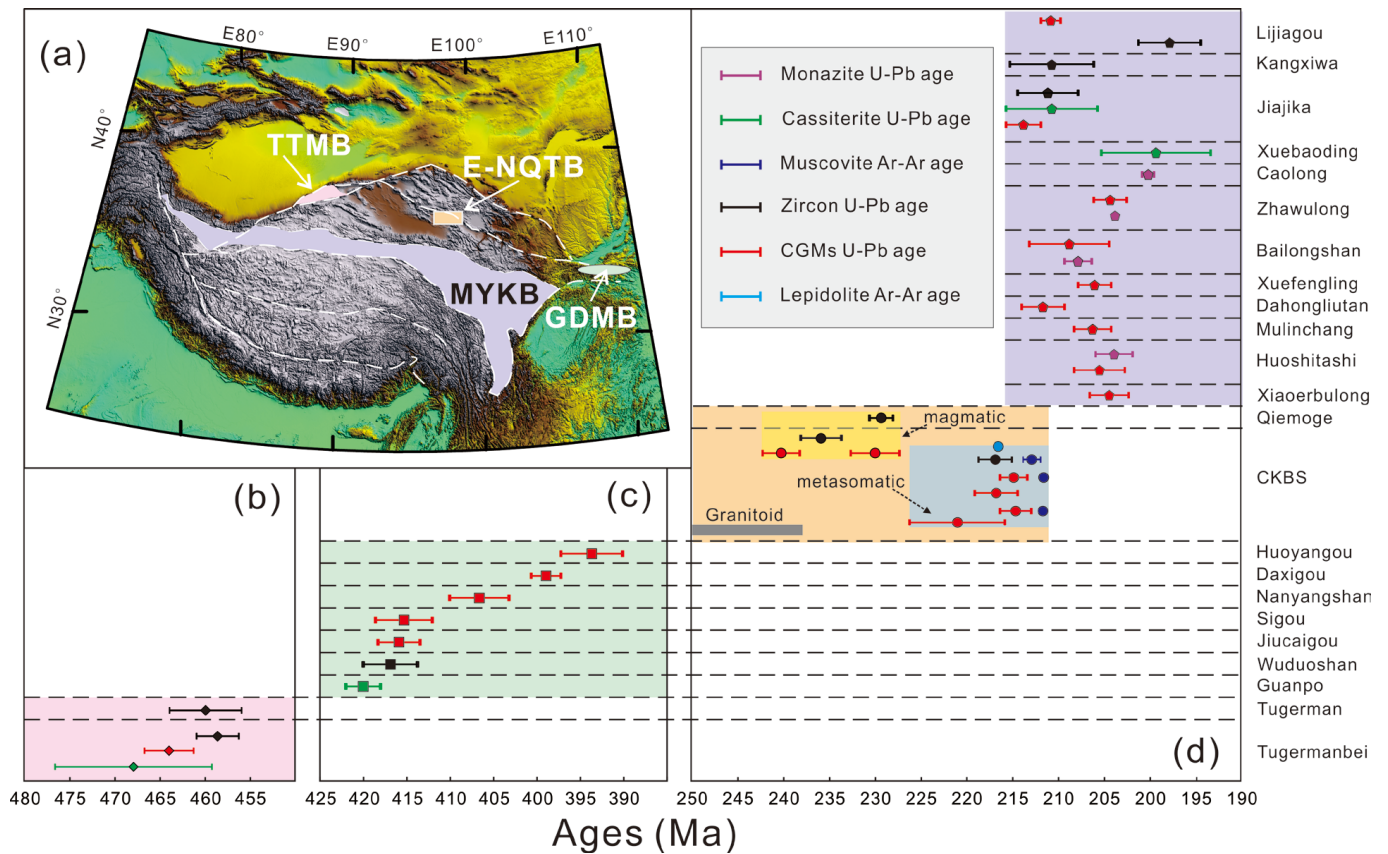


Figure 10. Comparison of geochronological data of the pegmatite-type rare-metal deposits in the TTMB, GDMB, E-NQTB and MYKB. (a) Topographic map showing the distributions of the rare-metal mineralized belts around the CKBS deposit in the eastern NQTB (modified after Zhan et al. [88], Zhang et al. [89] and Robinson [90]). (b) the dating results for the TTMB (Tugman-Tashisayi mineralization belt, pink area). (c) the dating results for the GDMB (Guanpo-Danfeng mineralization belt, laurel-green area). (d) the dating results for the E-NQTB (the eastern North Qaidam Tectonic Belt, saffron yellow area) and the MYKB (Markam-Yajiang-Karakoram belt, purple area). Yellow area and light grey area in (c) represent the ranges for crystallization ages and metasomatic ages of pegmatites in the eastern NQTB, respectively. Detailed data and sources are shown in Table 3. This diagram does not include the muscovite Ar-Ar ages of the Aketasi, Dangba and Tugmanbei deposits due to their far difference from the results of other geochronological methods. Meanwhile, due to the large error values (± 8 , MSWD = 6.7, Li et al. [23]), the cassiterite U-Pb age for the 505 Li is also ruled out. The ages of Triassic granitoids (grey area) in the eastern NQTB are from Wu et al. [91] and Sun et al. [42].

Table 3. The formation ages revealed by various dating methods for pegmatite-type rare-metal deposits in the TTMB, MYKB, GDMB and the eastern NQTB.

Deposit	Mineralized Belt	Dating Method	Age (Ma)	References
CKBS	The eastern NQTB	Columbite U-Pb *	230.1 ± 2.6	This study
		Columbite U-Pb *	240.6 ± 1.5	Pan et al. [4]
		Columbite U-Pb **	214.9 ± 1.7	Liu et al. [21]
		Columbite U-Pb **	217 ± 2.3	Liu et al. [21]
		Columbite U-Pb **	221.2 ± 5.3	This study
		Columbite U-Pb **	215 ± 1.5	Liu et al. [21]
		Zircon U-Pb	217 ± 1.8	Wang et al. [32]
		Zircon U-Pb	235.9 ± 2.3	Wang et al. [32]
		Muscovite Ar-Ar	212.6 ± 0.6	Chen et al. [44]
		Muscovite Ar-Ar	211.7 ± 0.4	Liu et al. [21]
		Muscovite Ar-Ar	211.8 ± 0.3	Liu et al. [21]
		Lepidolite Ar-Ar	216.6 ± 0.9	Liu et al. [21]
		Qiemoge	The eastern NQTB	Zircon U-Pb
Aketasi	MYKB	Muscovite Ar-Ar	144.7 ± 4.3	Qiao et al. [92]
505 Li	MYKB	Cassiterite U-Pb	223.5 ± 7.9	Li et al. [23]
Xiaoerbulong	MYKB	Columbite U-Pb	204.6 ± 2.1	Yan et al. [20]
Kangxiwar	MYKB	Zircon U-Pb	209 ± 4.4	Zhang et al. [93]
Xuefengling	MYKB	Columbite U-Pb	206.3 ± 1.8	Yan et al. [20]
Bailongshan	MYKB	Columbite U-Pb	208.1 ± 1.5	Wang et al. [94]
		Monazite U-Pb	207.4 ± 0.6	Yan et al. [20]
Caolong	MYKB	Monazite U-Pb	204 ± 0.3	Li et al. [87]
		Monazite U-Pb	200.4 ± 0.7	Li et al. [87]
Zhawulong	MYKB	Columbite U-Pb	204.5 ± 1.8	Li et al. [95]
Xuebaoding	MYKB	Cassiterite U-Pb	199.6 ± 6	Yan et al. [20]
		Jiajika	MYKB	Columbite U-Pb
		Cassiterite U-Pb	210.9 ± 4.6	Dai et al. [97]
		Zircon U-Pb	211 ± 5	Dai et al. [97]
		Dangba	MYKB	Muscovite Ar-Ar
Dahongliutan	MYKB	Columbite U-Pb	211.9 ± 2.4	Yan et al. [24]
Mulinchang	MYKB	Columbite U-Pb	206.4 ± 2.0	Yan et al. [20]
Huoshitashi	MYKB	Columbite U-Pb	205.7 ± 2.7	Yan et al. [20]
		Monazite U-Pb	204.2 ± 2.0	Yan et al. [20]
Lijiagou	MYKB	Zircon U-Pb	198 ± 3.4	Fei et al. [99]
		Columbite U-Pb	211.1 ± 1.0	Fei et al. [22]
Tugman	TTMB	Zircon U-Pb	459.9 ± 3.7	Xu et al. [85]
Tugmanbei	TTMB	Zircon U-Pb	458.7 ± 2.3	Li et al. [76]
		Cassiterite U-Pb	468 ± 8.7	Li et al. [76]
		Muscovite Ar-Ar	350.2 ± 1.6	Li et al. [76]
		Columbite U-Pb	464.1 ± 2.7	Li et al. [76]
Guanpo	GDMB	Cassiterite U-Pb	420 ± 2	Zeng et al. [83]
Wuduoshan	GDMB	Zircon U-Pb	417.4 ± 2.5	Chen et al. [100]
Nanyangshan	GDMB	Columbite U-Pb	406.8 ± 3.3	Yuan et al. [86]
Jiugaigou	GDMB	Columbite U-Pb	415.9 ± 2.4	Zhou et al. [16]
Daxigou	GDMB	Columbite U-Pb	399.2 ± 1.7	Zhou et al. [16]
Sigou	GDMB	Columbite U-Pb	415.4 ± 3.2	Zhou et al. [16]
Huoyangou	GDMB	Columbite U-Pb	393.9 ± 3.6	Zhou et al. [16]

* represents magmatic age; ** represents metasomatic age; NQTB: North Qaidam Tectonic Belt; MYKB: Markam-Yajiang-Karakoram Mineralization Belt; TTMB: Tugman-Tashisayi Mineralization Belt; GDMB: Guanpo-Danfeng Mineralization Belt.

Except for *ca.* 800 pegmatite dykes in the CKBS deposit, significantly abundant pegmatite dykes have also been found in the eastern segment of NQTB (Figure 11), e.g., *ca.* 360 in the Shaliuquan area, *ca.* 100 in the Chahannuo area and *ca.* 700 in the Shinaihai area [28,33]. Recently, several granite-pegmatite-related rare metal deposits/mineralization points have also been discovered in these pegmatite-exposure areas, including the Shaliuquan Nb-Ta deposit, Asiheta Be deposit, Shinaihai Nb-Ta-Rb deposit, Honglingbei Li-Be mineralization point, Yematannan Li mineralization point, and so on (Figure 11). In addition

to the pegmatite in the CKBS deposit, pegmatite dykes in other deposits/mineralized points in the eastern NQTB are very poorly understood, which makes it difficult to quantitatively decipher the rare-metal metallogenic regularity at the moment. However, the following three commonalities can be concluded for the pegmatite dykes in the eastern NQTB based on the results of preliminary field investigations [28–33,40]: (1) mostly intruded into schist, gneiss, and marble of Paleoproterozoic Dakendaban Group; (2) distributions were controlled by secondary fracture and/or ductile shear zone; (3) closed related to adjacent granite, some even occurred in granite. Therefore, we suggest that the eastern NQTB may be a new potential rare-metal mineralization belt, which should be explored in detail and arouse painstaking attention.

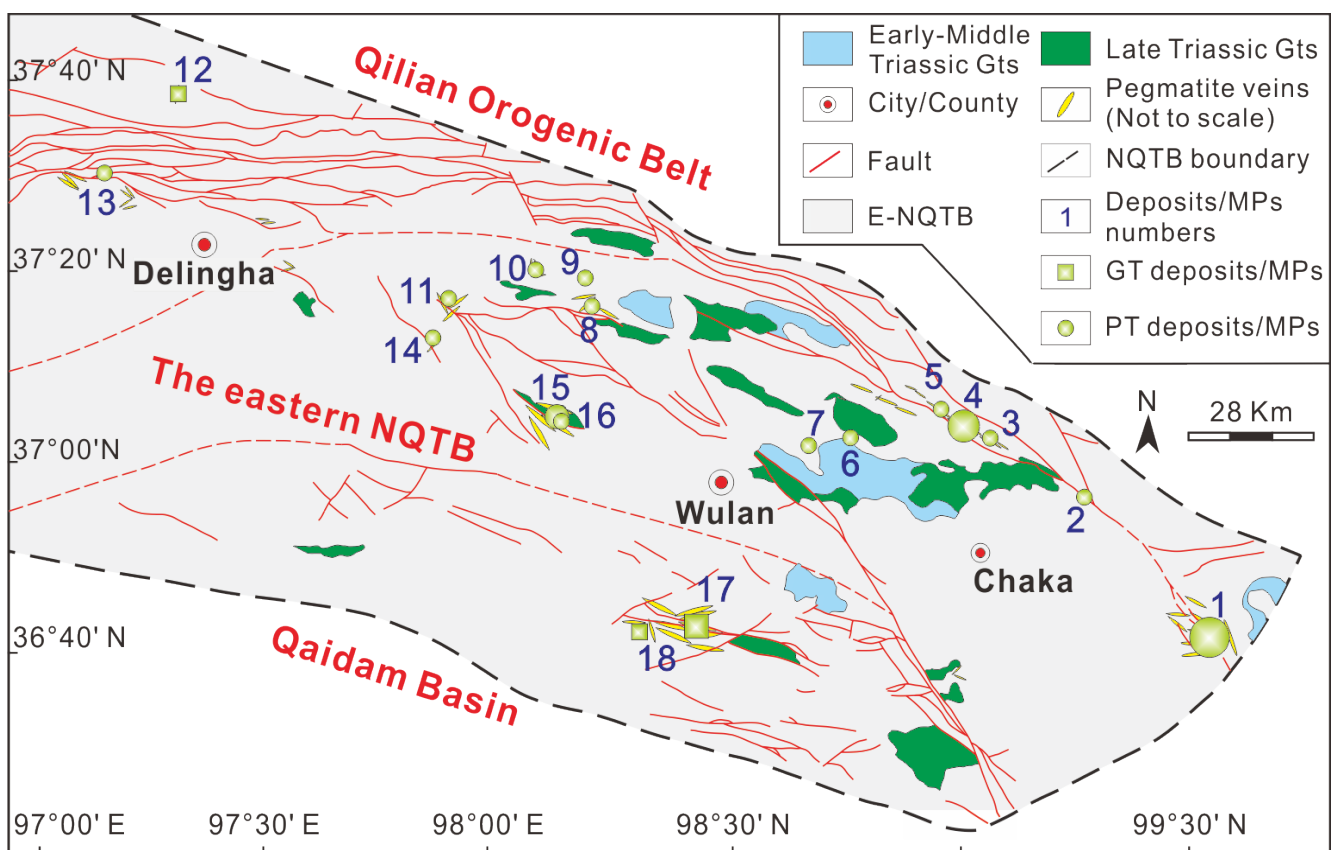


Figure 11. Geological sketch of Triassic granitoids and rare-metal deposits in the eastern NQTB. Letter abbreviations: NQTB = North Qaidam Tectonic Belt, Gts = granitoids, GT = granite-type, PT = pegmatite-type and MPs = mineralization points. Number abbreviations of deposits/mineralized-point: 1 = Shinaihai Nb-Ta deposit, 2 = Honglingbei Li mineralized point, 3 = Qiemoge Li-Be deposit, 4 = Chakabeishan Li-Be deposit, 5 = Edanggang Be deposit, 6 = Ashiheta Be deposit, 7 = Chahannuo Nb mineralized point, 8 = Shenge Nb mineralized point, 9 = Yematannan Nb-Ta mineralized point, 10 = Bahagaidege Be mineralized point, 11 = Gaotelameng REE mineralized point, 12 = Balegenluole LREE mineralized point, 13 = Chahansen Nb mineralized point, 14 = Halahada Be mineralized point, 15 = Shaliuquan Nb-Ta deposit, 16 = Amuneige Nb mineralized point, 17 = Xiaerdawu Nb-REE mineralized deposit, 18 = Chachaxiangka U mineralized point.

7. Conclusions

(1) Three-stage crystallizations of CGM crystals are identified in terms of variations in internal zoning patterns and major element compositions. First, oscillatory CGMs-1 ferrocolumbite grains crystallize at the magmatic stage, which are products of non-equilibrium fractional crystallization and are characterized by episodic variations in Ta/(Ta + Nb), TiO₂, WO₃ and PbO. Second, homogeneous CGMs-2 ferrocolumbite grains are formed at the magmatic-hydrothermal transition stage, which result from equilibrium

crystallization via fluid-melt interactions and are characterized by the relatively stable Ta/(Ta + Nb) and moderately elevated Mn/(Mn + Fe). Third, irregular/complex CGMs-3 crystals commonly consist of Nb-rich domains (CGMs-3a) and Ta-rich domains (CGMs-3b) and are formed by the metasomatism of early-formed CGMs-1 and CGMs-2 with special fluids. This metasomatism causes considerably elevated Ta/(Ta + Nb) in CGMs-3b.

(2) The investigated spodumene pegmatite dyke (No.15) emplaced at 230.1 ± 2.6 Ma and then experienced a late fluid-induced metasomatic event at 221 ± 5.3 Ma.

(3) The CKBS deposit is not likely to be connected to the adjacent rare-metal mineralization belts (MYKB, GDTB and TTMB). The occurrence of abundant pegmatite dykes and obvious mineralization information indicate that the eastern NQTB may be a new potential rare-metal mineralization belt in western China, which should be paid more attention to.

Supplementary Materials: The following supporting information can be downloaded at: <https://www.mdpi.com/article/10.3390/min13020201/s1>, Table S1: Chemical compositions of CGMs in the spodumene pegmatite from the CKBS Li-Be deposit analyzed by EMPA.

Author Contributions: Conceptualization, W.S., Z.Z. and X.M.; Data Curation, W.S.; Writing-Original Draft, W.S.; Writing-Review & Editing, Z.Z.; Validation, S.Y. and L.Z.; Supervision, Z.Z., X.M., C.W., B.W. and T.P.; Project Administration, Z.Z., X.M., G.D., X.L., W.Y. and T.W.; Funding Acquisition, Z.Z.; Investigation, W.S., Z.Z., G.D., W.Y., T.W., B.W., J.H., H.C. and Y.T. All authors have read and agreed to the published version of the manuscript.

Funding: The present study was financially supported by the National Natural Science Foundation of China (Grant No. 92062217) and the University Innovation Foundation of Education Department of Gansu Province (Grant No. 2021A-230).

Data Availability Statement: The authors declare that all analytical data supporting the findings of this study are available within the paper and its supplementary information files or cited peer-review references.

Acknowledgments: We are indebted to Yao Wang from the China University of Geosciences for his work with rock samples preparation. We sincerely thank Zhenzhong Liu and Weilin La from the Bureau of Geological Exploration and Development of Qinghai Province for their help in the field investigation. We are also grateful to the editors and reviewers for their constructive comments that led to significant improvements in the manuscript.

Conflicts of Interest: The authors declare no conflict of interest.

References

1. Gulley, A.L.; Nassar, N.T.; Xun, S. China, the United States, and competition for resources that enable emerging technologies. *Proc. Natl. Acad. Sci. USA* **2018**, *115*, 4111–4115. [[CrossRef](#)] [[PubMed](#)]
2. Wang, D.H. Discussion on issues related to strategic key mineral resource. *Geol. Chem. Miner.* **2019**, *41*, 65–72. (In Chinese with English abstract)
3. Wang, D.H. Study on critical mineral resources: Significance of research, determination of types, attributes of resources, progress of prospecting, problems of utilization and direction of exploitation. *Acta Geol. Sin.* **2019**, *93*, 1189–1209. (In Chinese with English abstract)
4. London, D. Ore-forming processes within granitic pegmatites. *Ore Geol. Rev.* **2018**, *101*, 349–383. [[CrossRef](#)]
5. Zhang, A.C.; Wang, R.C.; Hu, H.; Zhang, H.; Zhu, J.C.; Chen, X.M. Chemical evolution of Nb-Ta oxides and zircon from the Koktokay No.3 granitic pegmatite, Altai, northwestern China. *Mineral. Mag.* **2004**, *68*, 739–756. [[CrossRef](#)]
6. Linnen, R.L.; van Lichtenvelde, M.; Černý, P. Granitic pegmatites as sources of strategic metals. *Elements* **2012**, *8*, 275–280. [[CrossRef](#)]
7. Sun, W.L.; Liu, Y.; Zhang, Z.W. Research progress on petrogenesis of LCT-type granitic pegmatite and therein lithium enrichment mechanism. *Northwest. Geol.* **2022**, *55*, 35–55. (In Chinese with English abstract)
8. Chukwu, A.; Obiora, S.C. Petrogenetic characterization of pegmatites and their host rocks in southern Akwanga, North-Central Basement Complex, Nigeria. *J. Earth Syst. Sci.* **2021**, *130*, 18. [[CrossRef](#)]
9. Maneta, V.; Baker, D.R. The potential of lithium in alkali feldspars, quartz, and muscovite as a geochemical indicator in the exploration for lithium-rich granitic pegmatites: A case study from the spodumene-rich Moblan pegmatite, Quebec, Canada. *J. Geochem. Explor.* **2019**, *205*, 106336. [[CrossRef](#)]
10. London, D. Reply to Thomas and Davidson on “A petrologic assessment of internal zonation in granitic pegmatites” (London, 2014a). *Lithos* **2015**, *212*, 469–484. [[CrossRef](#)]

11. Thomas, R.; Davidson, P. Comment on “A petrologic assessment of internal zonation in granitic pegmatites” by David London (2014). *Lithos* **2015**, *212*, 462–468. [[CrossRef](#)]
12. Thomas, R.; Davidson, P.; Beurlen, H. The competing models for the origin and internal evolution of granitic pegmatites in the light of melt and fluid inclusion research. *Miner. Petrol.* **2012**, *106*, 55–73. [[CrossRef](#)]
13. Trumbull, R.B.; Beurlen, H.; Wiedenbeck, M.; Soares, D.R. The diversity of B-isotope variations in tourmaline from rare-element pegmatites in the Borborema Province of Brazil. *Chem. Geol.* **2013**, *352*, 47–62. [[CrossRef](#)]
14. van Hinsberg, V.J.; Henry, D.J.; Marschall, H.R. Tourmaline: An ideal indicator of its host environment. *Can. Mineral.* **2011**, *49*, 1–16. [[CrossRef](#)]
15. Hulsbosch, N.; Hertogen, J.; Dewaele, S.; André, L.; Muchez, P. Alkali metal and rare earth element evolution of rock-forming minerals from the Gatumba area pegmatites (Rwanda): Quantitative assessment of crystal-melt fractionation in the regional zonation of pegmatite groups. *Geochim. Cosmochim. Acta* **2014**, *132*, 349–374. [[CrossRef](#)]
16. Zhou, Q.F.; Qin, K.Z.; Tang, D.M.; Wang, C.L. A combined EMPA and LA-ICP-MS study of muscovite from pegmatites in the Chinese Altai, NW China: Implications for tracing rare-element mineralization type and ore-forming process. *Minerals* **2022**, *12*, 377. [[CrossRef](#)]
17. Černý, P.; Ercit, T.S. Some recent advances in the mineralogy and geochemistry of Nb and Ta in rare-element granitic pegmatites. *Bull. Mineral.* **1985**, *108*, 499–532. [[CrossRef](#)]
18. Černý, P.; Ercit, T.S. Mineralogy of niobium and tantalum: Crystal chemical relationships, paragenetic aspects and their economic implications. In *Lanthanides, Tantalum and Niobium*; Moller, P., Černý, P., Saupe, F., Eds.; Springer: Berlin, Germany, 1989; pp. 27–79.
19. Tindle, A.G.; Breaks, F.W. Columbite-tantalite mineral chemistry from rare-element granitic pegmatites: Separation Lakeh area, NW Ontario, Canada. *Miner. Petrol.* **2000**, *70*, 165–198. [[CrossRef](#)]
20. Yan, Q.H.; Wang, H.; Chi, G.; Wang, Q.; Hu, H.; Zhou, K.L.; Zhang, X.Y. Recognition of a 600-km long late Triassic rare metal (Li-Rb-Be-Nb-Ta) pegmatite belt in the western Kunlun Orogenic belt, western China. *Econ. Geol.* **2022**, *117*, 213–236. [[CrossRef](#)]
21. Liu, J.H.; Wang, Q.; Xu, C.B.; Zhou, J.S.; Wang, B.Z.; Li, W.F.; Li, S.P.; Huang, T.Y.; Yan, Q.H.; Song, B.Z.; et al. Geochronology of the Chakabeishan Li-(Be) rare-element pegmatite, Zongwulong orogenic belt, northwest China: Constraints from columbite-tantalite U-Pb and muscovite-lepidolite $^{40}\text{Ar}/^{39}\text{Ar}$ dating. *Ore Geol. Rev.* **2022**, *146*, 104930. [[CrossRef](#)]
22. Fei, G.C.; Menuge, J.F.; Li, Y.Q.; Yang, J.Y.; Deng, Y.; Chen, C.S.; Yang, Y.F.; Yang, Z.; Qin, L.Y.; Zheng, L.; et al. Petrogenesis of the Lijiagou spodumene pegmatites in Songpan-Garze fold belt, West Sichuan, China: Evidence from geochemistry, zircon, cassiterite and coltan U-Pb geochronology and Hf isotopic compositions. *Lithos* **2020**, *364*, 105555. [[CrossRef](#)]
23. Li, K.; Gao, Y.B.; Teng, J.X.; Jin, M.S.; Li, W. Metallogenic geological characteristics, mineralization age and resource potential of the granite-pegmatite-type rare metal deposits in Dahongliutan area, Hetian County, Xinjiang. *Northwest. Geol.* **2019**, *52*, 206–221. (In Chinese with English abstract)
24. Yan, Q.H.; Qiu, Z.W.; Wang, H.; Wang, M.; Wei, X.P.; Li, P.; Zhang, R.Q.; Li, C.Y.; Liu, J.P. Age of the Dahongliutan rare metal pegmatite deposit, West Kunlun, Xinjiang (NW China): Constraints from LA-ICP-MS U-Pb dating of columbite-(Fe) and cassiterite. *Ore Geol. Rev.* **2018**, *100*, 561–573. [[CrossRef](#)]
25. Xu, Z.Q.; Fu, X.F.; Wang, R.C.; Li, G.W.; Zheng, Y.L.; Zhao, Z.B.; Lian, D.Y. Generation of lithium-bearing pegmatite deposits within the Songpan-Ganze orogenic belt, East Tibet. *Lithos* **2020**, *354*, 105281. [[CrossRef](#)]
26. Yue, Y.; Sun, D.Y.; Hou, K.J.; Peng, Y.B. Geochronology and geochemistry of Triassic gabbro in Northern Wulan, northern margin of Qaidam Basin. *J. Jilin Univ. (Earth Sci.)* **2021**, *51*, 154–168. (In Chinese with English abstract)
27. Wu, C.L.; Wu, D.; Mattinson, C.; Lei, M.; Chen, H.J. Petrogenesis of granitoids in the Wulan area: Magmatic activity and tectonic evolution in the North Qaidam, NW China. *Gondwana Res.* **2019**, *67*, 147–171. [[CrossRef](#)]
28. Pan, T.; Li, S.P.; Ren, H.; Wang, B.Z.; Li, W.F.; Wang, C.T.; Jin, T.T. Metallogenic conditions and prospecting potential of Lithium polymetallic deposits in North Qaidam Basin. *Miner. Explor.* **2020**, *11*, 1101–1116. (In Chinese with English abstract)
29. Li, S.P.; Pan, T.; Wang, B.Z.; Yan, X.P.; Ren, H.; Yu, F.C.; Qiu, W.; Wang, J.J.; Tang, J.; Wang, J.S.; et al. Characteristics and tectonic significance of Beryl-bearing pegmatites in Qiemoge Mountain, Northern margin of Qaidam Basin. *Geotecton. Metallog.* **2021**, *45*, 608–619. (In Chinese with English abstract)
30. Li, S.P.; Ren, H.; Wang, C.T.; Li, W.F.; Wang, J.S.; Wang, J.F.; Jin, T.T.; Sun, H.L. Indosinian tectonic setting, magmatism and rare metal mineralization in the northern marginal area of Qaidam Basin. *J. Salt Lake Res.* **2020**, *28*, 1–9. (In Chinese with English abstract)
31. Pan, T.; Li, S.P.; Wang, T.; Han, G.; Jia, J.T. Metallogenic characteristics and prospecting potential of lithium deposits in the Qinghai Province. *Acta Geol. Sin.* **2022**, *96*, 1827–1854. (In Chinese with English abstract)
32. Wang, B.Z.; Han, J.; Xie, X.L.; Chen, J.; Wang, T.; Xue, W.W.; Bai, Z.H.; Li, S.P. Discovery of the Indosinian (Beryl-bearing) spodumene pegmatitic dike swarm in the Chakaibeishan area in the northeastern margin of the Tibetan plateau: Implications for Li-Be mineralization. *Geotecton. Metallog.* **2020**, *44*, 69–79. (In Chinese with English abstract)
33. Li, S.P.; Xue, W.W.; Ren, H.; Zhao, H.X.; Zhang, Z.Q.; Qiu, W.; Cheng, B.F.; Bai, J.H.; Fu, J. The status and metallogenic regularity of critical mineral resource in Qinghai Province, China. *Qinghai Technol.* **2018**, *6*, 10–15. (In Chinese)
34. Chen, N.S.; Lu, Z.; Min, S.; Wang, Q.Y.; Kusky, T.M. U-Pb and Hf isotopic compositions of detrital zircons from the paragneisses of the Quanji Massif, NW China: Implications for its early tectonic evolutionary history. *J. Asian Earth Sci.* **2012**, *54–55*, 110–130. [[CrossRef](#)]

35. Li, X.C.; Niu, M.L.; Yakymchuk, C.; Yan, Z.; Fu, C.L.; Zhao, Q.Q. Anatexis of former arc magmatic rocks during oceanic subduction: A case study from the north Wulan gneiss complex. *Gondwana Res.* **2018**, *61*, 128–149. [[CrossRef](#)]
36. Ren, Y.F.; Chen, D.L.; Wang, H.J.; Zhu, X.H.; Bai, B.W. Grenvillian and early paleozoic polyphase metamorphism recorded by eclogite and host garnet mica schist in the north Qaidam Orogenic belt. *Geosci. Front.* **2021**, *12*, 101170. [[CrossRef](#)]
37. Wu, C.L.; Gao, Y.H.; Li, Z.L.; Lei, M.; Qin, H.P.; Li, M.Z.; Liu, C.H.; Ronald, B.F.; Paul, T.R.; Joseph, L.W. Zircon SHRIMP U-Pb dating of granites from Dulan and the chronological framework of the North Qaidam UHP belt, NW China. *Sci. China Earth Sci.* **2014**, *57*, 2945–2965. [[CrossRef](#)]
38. Song, S.G.; Niu, Y.L.; Su, L.; Zhang, C.; Zhang, L.F. Continental orogenesis from ocean subduction, continent collision/subduction, to orogen collapse, and orogen recycling: The example of the North Qaidam UHPM belt, NW China. *Earth Sci. Rev.* **2014**, *129*, 59–84. [[CrossRef](#)]
39. Zhang, L.; Wang, Q.Y.; Chen, N.S.; Sun, M.; Santosh, M.; Ba, J. Geochemistry and detrital zircon U-Pb and Hf isotopes of the paragneiss suite from the Quanji Massif, SE Tarim Craton: Implication for Paleoproterozoic tectonics in NW China. *J. Asian Earth Sci.* **2014**, *95*, 33–50. [[CrossRef](#)]
40. Pan, T.; Ding, Q.F.; Zhou, X.; Li, S.P.; Han, J.; Cheng, L. Columbite-Tantalite Group Mineral U-Pb Geochronology of Chaqiabeishan Li-Rich Granitic Pegmatites in the Quanji Massif, NW China: Implications for the Genesis and Emplacement Ages of Pegmatites. *Front. Earth Sci.* **2021**, *8*, 606951. [[CrossRef](#)]
41. Liu, C.X.; Sun, F.Y.; Qian, Y.; Wu, D.Q.; Hui, C.; Lu, Y.H. Vertical zonation characteristics of Chakabeishan Li-Be rare-metal pegmatite deposit in northern margin of Qaidam Basin, Qinghai Province. *Glob. Geol.* **2021**, *40*, 843–880. (In Chinese with English abstract)
42. Sun, W.L.; Zhao, Z.D.; Mo, X.X.; Wei, C.J.; Dong, G.C.; Li, X.W.; Yuan, W.M.; Wang, T.; Wang, B.Z.; Pan, T.; et al. Petrogenesis of pegmatite revealed by geochemical and Hf isotopic data: A case study from the eastern North Qaidam Tectonic Belt, northern Tibetan Plateau. *Geochemistry*, 2022, submitted.
43. Sun, W.L.; Zhao, Z.D.; Niu, Y.L.; Wei, C.J.; Dong, G.C.; Li, X.W.; Yuan, W.M.; Wang, T.; Wang, B.Z.; Pan, T.; et al. Petrogenesis of regionally zoned pegmatite and associated Li-Be enrichment process: Perspectives from major-element and B isotopic composition of tourmaline. *Geosci. Front.* 2022, submitted.
44. Chen, J.; Han, J.; Yu, F.C.; Wang, B.Z.; Li, W.F. ⁴⁰Ar-³⁹Ar dating of muscovite in Chaka Beishan Li-polymetallic deposit in Qinghai Province and the geological significance. *Contrib. Geol. Miner. Resource Res.* **2022**, *37*, 142–147. (In Chinese with English abstract)
45. Che, X.D.; Wu, F.Y.; Wang, R.C.; Gerdes, A.; Ji, W.Q.; Zhao, Z.H.; Yang, H.H.; Zhu, Z.Y. In situ U-Pb isotopic dating of columbite-tantalite by LA-ICP-MS. *Ore Geol. Rev.* **2015**, *65*, 979–989. [[CrossRef](#)]
46. Ludwig, K.R. *Users Manual for Isoplot Version 3.75–4.15: A Geochronological Tool Kit for Microsoft Excel. 4*; Berkeley Geochronological Centre Special Publication: Berkeley, CA, USA, 2012; p. 75.
47. Zhao, Z.; Yang, X.; Lu, S.; Lu, Y.; Sun, C.; Chen, S.; Chen, S.S.; Zhang, Z.Z.; Bute, S.I.; Zhao, L.L. Genesis of Late Cretaceous granite and its related Nb-Ta-W mineralization in Shangbao, Nanling Range: Insights from geochemistry of whole-rock and Nb-Ta minerals. *Ore Geol. Rev.* **2021**, *131*, 103975. [[CrossRef](#)]
48. Sami, M.; Ntaflos, T.; Farahat, E.S.; Mohamed, H.A.; Ahmed, A.F.; Hauzenberger, C. Mineralogical, geochemical and Sr-Nd isotopes characteristics of fluorite-bearing granites in the Northern Arabian-Nubian Shield, Egypt: Constraints on petrogenesis and evolution of their associated rare metal mineralization. *Ore Geol. Rev.* **2017**, *88*, 1–22. [[CrossRef](#)]
49. van Lichtenvelde, M.; Salvi, S.; Beziat, D.; Linnen, R.L. Textural features and chemical evolution in tantalum oxides: Magmatic versus hydrothermal origins for Ta mineralization in the Tanco Lower Pegmatite, Manitoba, Canada. *Econ. Geol.* **2007**, *102*, 257–276. [[CrossRef](#)]
50. McNeil, A.G.; Linnen, R.L.; Flemming, R.L.; Fayek, M. An experimental approach to examine fluid-melt interaction and mineralization in rare-metal pegmatites. *Am. Mineral.* **2020**, *105*, 1078–1087. [[CrossRef](#)]
51. Diao, X.; Wu, M.; Zhang, D.; Liu, J. Textural features and chemical evolution of Ta-Nb-W-Sn oxides in the Jianfengling Deposit, South China. *Ore Geol. Rev.* **2022**, *142*, 104690. [[CrossRef](#)]
52. González, T.L.; Polonio, F.G.; Moro, F.J.L.; Fernández, A.F.; Contreras, J.L.S.; Benito, M.C.M. Tin-tantalum-niobium mineralization in the Penouta deposit (NW Spain): Textural features and mineral chemistry to unravel the genesis and evolution of cassiterite and columbite group minerals in a peraluminous system. *Ore Geol. Rev.* **2017**, *81*, 79–95. [[CrossRef](#)]
53. Chládek, Š.; Uher, P.; Novák, M. Compositional and textural variations of columbite-group minerals from beryl-columbite pegmatites in the Maršíkov District, Bohemian Massif, Czech Republic: Magmatic versus hydrothermal evolution. *Can. Mineral.* **2020**, *58*, 767–783. [[CrossRef](#)]
54. Wu, M.; Samson, I.M.; Zhang, D.H. Textural features and chemical evolution in Ta-Nb oxides: Implications for deuteric rare-metal mineralization in the Yichun granite-marginal pegmatite, southeastern China. *Econ. Geol.* **2018**, *113*, 937–960. [[CrossRef](#)]
55. Timofeev, A.; Williams-Jones, A.E. The origin of niobium and tantalum mineralization in the Nechalacho REE Deposit, NWT, Canada. *Econ. Geol.* **2015**, *110*, 1719–1735. [[CrossRef](#)]
56. Lahti, S.I. Zoning in columbite-tantalite crystals from the granitic pegmatites of the Eräjärvi area, southern Finland. *Geochim. Cosmochim. Acta* **1987**, *51*, 509–517. [[CrossRef](#)]
57. Chudík, P.; Uher, P.; Gadas, P.; Škoda, R.; Pršek, J. Niobium-tantalum oxide minerals in the Jezuitské Lesy granitic pegmatite, Bratislava Massif, Slovakia: Ta to Nb and Fe to Mn evolutionary trends in a narrow Be, Cs-rich and Li, B-poor dike. *Mineral. Petrol.* **2011**, *102*, 15–27. [[CrossRef](#)]

58. van Lichtervelde, M.; Linnen, R.L.; Salvi, S.; Beziat, D. The role of metagabbro rafts on tantalum mineralization in the Tanco granitic pegmatite, Manitoba. *Can. Mineral.* **2006**, *44*, 625–644. [[CrossRef](#)]
59. van Lichtervelde, M.; Holtz, F.; Melcher, F. The effect of disequilibrium crystallization on Nb-Ta fractionation in pegmatites: Constraints from crystallization experiments of tantalite-tapiolite. *Am. Mineral.* **2018**, *103*, 1401–1416. [[CrossRef](#)]
60. McNeil, A.G. Crystallization Processes and Solubility of Columbite-(Mn), Tantalite-(Mn), Microlite, Pyrochlore, Wodginite and Titanowodginite in Highly Fluxed Haplogranitic Melts. Ph.D. Thesis, The Western University, London, UK, 2018.
61. Zhou, Z.; Breiter, K.; Wilde, S.A.; Gao, X.; Burnham, A.D.; Ma, X.; Zhao, J. Ta-Nb mineralization in the shallow-level highly-evolved P-poor Shihuiyao granite, Northeast China. *Lithos* **2022**, *416*, 106655. [[CrossRef](#)]
62. Jahns, R.H.; Burnham, C.W. Experimental studies of pegmatite genesis: I. A model for the derivation and crystallization of granitic pegmatites. *Econ. Geol.* **1969**, *64*, 843–864. [[CrossRef](#)]
63. Manning, D.A.C. Chemical and morphological variation in tourmalines from the Hub Kapong batholith of peninsular Thailand. *Mineral. Mag.* **1982**, *45*, 139–147. [[CrossRef](#)]
64. Borodulin, G.P.; Chevychelov, V.Y.; Zaraysky, G.P. Experimental study of partitioning of tantalum, niobium, manganese, and fluorine between aqueous fluoride fluid and granitic and alkaline melts. *Doklady Earth Sci.* **2009**, *427*, 868–873. [[CrossRef](#)]
65. Borisova, A.Y.; Thomas, R.; Salvi, S.; Candaudap, F.; Lanzanova, A.; Chmeleff, J. Tin and associated metal and metalloid geochemistry by femtosecond LA-ICP-QMS microanalysis of pegmatite–leucogranite melt and fluid inclusions: New evidence for melt–melt–fluid immiscibility. *Mineral. Mag.* **2012**, *76*, 91–113. [[CrossRef](#)]
66. Kotelnikov, A.R.; Korzhinskaya, V.S.; Kotelnikova, Z.A.; Suk, N.I. Influence of silicate substance on Pyrochlore and Tantalite solubility in fluoride aqueous solutions (experimental studies). *Russ. Geol. Geophys.* **2020**, *61*, 26–35.
67. Timofeev, A.; Migdisov, A.A.; Williams-Jones, A.E. An experimental study of the solubility and speciation of tantalum in fluoride-bearing aqueous solutions at elevated temperature. *Geochim. Cosmochim. Acta* **2017**, *197*, 294–304. [[CrossRef](#)]
68. Zaraysky, G.P.; Korzhinskaya, V.; Kotova, N. Experimental studies of Ta₂O₅ and columbite–tantalite solubility in fluoride solutions from 300 to 550 °C and 50 to 100 MPa. *Miner. Petrol.* **2010**, *99*, 287–300. [[CrossRef](#)]
69. Shaw, R.A.; Goodenough, K.M.; Deady, E.; Nex, P. The magmatic-hydrothermal transition in lithium pegmatites: Petrographic and geochemical characteristics of pegmatites from the Kamativi area, Zimbabwe. *Can. Mineral.* **2022**, *60*, 1–31. [[CrossRef](#)]
70. Llera, A.R.; Fuertes-Fuente, M.; Cepedal, A.; Martin-Izard, A. Barren and Li-Sn-Ta mineralized pegmatites from NW Spain (Central Galicia): A comparative study of their mineralogy, geochemistry, and wallrock metasomatism. *Minerals* **2019**, *9*, 739. [[CrossRef](#)]
71. Sami, M.; El Monsef, M.A.; Abart, R.; Toksoy-koksal, F.; Abdelfadil, K.M. Unraveling the genesis of highly fractionated rare-metal granites in the Nubian shield via the rare-earth elements tetrad effect, Sr-Nd isotope systematic and mineral chemistry. *ACS Earth Space Chem.* **2022**, *6*, 2368–2384. [[CrossRef](#)]
72. Madayipu, N.; Li, H.; Algeo, T.J.; Elatikpo, S.M.; Heritier, R.N.; Zhou, H.X.; Zheng, H.; Wu, Q.H. Long-lived Nb-Ta mineralization in Mufushan, NE Hunan, South China: Geological, geochemical, and geochronological constraints. *Geosci. Front.* **2023**, *14*, 101491. [[CrossRef](#)]
73. Zhou, Q.F.; Qin, K.Z.; Tang, D.M. Mineralogy of columbite-group minerals from the rare-element pegmatite veins in the East-Qinling orogen, central China: Implications for formation times and ore genesis. *J. Asian Earth Sci.* **2021**, *218*, 104879. [[CrossRef](#)]
74. Černý, P.; Novak, M.; Chapman, R. Effects of sillimanite-grade metamorphism and shearing on Nb-Ta oxide minerals in granitic pegmatites: Marsikov, Northern Moravia, Czechoslovakia. *Can. Mineral.* **1992**, *30*, 699–718.
75. Alfonso, P.; Melgarejo, J.C. Fluid evolution in the zoned rare-element pegmatite field at Cap de Creus, Catalonia, Spain. *Can. Mineral.* **2008**, *46*, 597–617. [[CrossRef](#)]
76. Li, H.; Hong, T.; Yang, Z.Q.; Chen, J.Z.; Ke, Q.; Wang, X.H.; Niu, L.; Xu, X.W. Comparative studying on zircon, cassiterite and coltan U-Pb dating and ⁴⁰Ar/³⁹Ar dating of muscovite rare-metal granitic pegmatite: A case study of the northern Tugman lithium-beryllium deposit in the middle of Altyn Tagh. *Acta Petrol. Sin.* **2020**, *36*, 2869–2892. (In Chinese with English abstract)
77. Burt, A.C.; Phillips, D. ⁴⁰Ar/³⁹Ar dating of muscovite from a pegmatite in Kinchina Quarry, near Murray Bridge. *MESA J.* **2003**, *28*, 50–52.
78. Zhou, J.S.; Wang, Q.; Xu, Y.G.; Cempirek, J.; Wang, H.; Ma, J.L.; Wei, G.J.; Huang, T.Y.; Zhu, G.H.; Zhang, L. Geochronology, petrology, and lithium isotope geochemistry of the Bailongshan granite-pegmatite system, northern Tibet: Implications for the ore-forming potential of pegmatites. *Chem. Geol.* **2021**, *584*, 120484. [[CrossRef](#)]
79. Černý, P. Rare-element granitic pegmatites. Part II: Regional to global environments and petrogenesis. *Geosci. Can.* **1991**, *18*, 68–81.
80. Roda-Robles, E.; Pesquera, A.; Velasco, F.; Fontan, F. The granitic pegmatites of the Fregeneda area (Salamanca, Spain); characteristics and petrogenesis. *Mineral. Mag.* **1999**, *63*, 535–558. [[CrossRef](#)]
81. Coleman, D.S.; Gray, W.; Glazner, A.F. Rethinking the emplacement and evolution of zoned plutons: Geochronologic evidence for incremental assembly of the Tuolumne Intrusive Suite, California. *Geology* **2004**, *32*, 433–436. [[CrossRef](#)]
82. Ghasemi Siani, M.; Mehrabi, B.; Bayat, S.; Neubauer, F.; Cao, S.Y. Geochronology, geochemistry and mineral chemistry of Malayer–Boroujerd–Shazand pegmatite dikes, Sanandaj–Sirjan zone, NW Iran. *Int. J. Earth Sci.* **2021**, *110*, 1139–1167. [[CrossRef](#)]

83. Zeng, W.; Sun, F.Y.; Zhou, H.Y.; Wang, J.Y.; Li, Z.D.; Chen, J.Q.; Bi, J.H.; Cui, Y.R. Cassiterite U-Pb age, geochemistry and their geological significances of rare metal pegmatites in Guanpo area, North Qinling, China. *Earth Sci.* **2021**, 1–30. (In Chinese with English abstract) [[CrossRef](#)]
84. Li, J.K.; Zou, T.R.; Liu, X.F.; Wang, D.H.; Ding, X. The metallogenetic regularities of lithium deposits in China. *Acta Geol. Sin-Engl.* **2015**, *89*, 652–670.
85. Xu, X.W.; Li, H.; Shi, F.P.; Yao, F.J.; Chen, J.Z.; Hong, T.; Ke, Q. Metallogenic characteristics and prospecting of granitic pegmatite-type rare metal deposits in the Tugman area, middle part of Altyn Tagh. *Acta Petrol. Sin.* **2019**, *35*, 3303–3316. (In Chinese with English abstract)
86. Yuan, F.; Jiang, S.Y.; Wang, C.L.; Jin, G.; Zhang, J.; Zhang, H.X.; Hu, X.J. U-Pb geochronology of columbite-group mineral, cassiterite, and zircon and Hf isotopes for Devonian rare-metal pegmatite in the Nanyangshan deposit, North Qinling Orogenic Belt, China. *Ore Geol. Rev.* **2022**, *140*, 104634. [[CrossRef](#)]
87. Li, W.F.; Li, S.P.; Wang, B.Z.; Wang, C.T.; Liu, J.H.; Zhang, X.Y.; Cao, J.S.; Xu, C.B.; Liu, J.D.; Jin, T.T. Discovery of the (Beryl-bearing) spodumene pegmatite in the Caolong area in the Sanjiang northern section of the Qinghai: Implication for Li-Be Mineralization. *Geotecton. Metallog.* **2021**, 1–25. (In Chinese with English abstract) [[CrossRef](#)]
88. Zhan, Q.Y.; Zhu, D.C.; Wang, Q.; Weinberg, R.F.; Xie, J.C.; Li, S.M.; Zhang, L.L.; Zhao, Z.D. Source and pressure effects in the genesis of the Late Triassic high Sr/Y granites from the Songpan-Ganzi Fold Belt, eastern Tibetan Plateau. *Lithos* **2020**, *368*, 105584. [[CrossRef](#)]
89. Zhang, C.L.; Zou, H.B.; Ye, X.T.; Chen, X.Y. Tectonic evolution of the West Kunlun Orogenic Belt along the northern margin of the Tibetan Plateau: Implications for the assembly of the Tarim terrane to Gondwana. *Geosci. Front.* **2019**, *10*, 973–988. [[CrossRef](#)]
90. Robinson, A.C. Geologic offsets across the northern Karakorum fault: Implications for its role and terrane correlations in the western Himalayan-Tibetan orogen. *Earth Planet. Sci. Lett.* **2009**, *279*, 123–130. [[CrossRef](#)]
91. Wu, C.L.; Lei, M.; Wu, D.; Li, T.X. Zircon SHRIMP dating and genesis of granites in Wulan area of northern Qaidam. *Acta GeoScientifica Sin.* **2016**, *37*, 493–516.
92. Qiao, G.B.; Wu, Y.Z.; Liu, T. Formation age of the Dahongliutan pegmatite type rare-metal deposit in Western Kunlun Mountains: Evidence from muscovite $^{40}\text{Ar}/^{39}\text{Ar}$ isotopic dating. *Geol. Chin.* **2020**, *47*, 1591–1593. (In Chinese)
93. Zhang, Z.; Liang, T.; Feng, Y.G.; Yang, X.Q.; Li, K.; Ding, K.; Wang, Y.Q. Geological Feature and Chronology Study of Kangxiwar Beryl-Bearing Muscovite Pegmatite in Weste Kunlun Orogen, Xinjiang. *Northwest. Geol.* **2019**, *52*, 75–88. (In Chinese with English abstract)
94. Wang, H.; Gao, H.; Zhang, X.Y.; Yan, Q.H.; Xu, Y.G.; Zhou, K.L.; Dong, R.; Li, P. Geology and geochronology of the super-large Bailongshan Li-Rb-(Be) rare-metal pegmatite deposit, West Kunlun orogenic belt, NW China. *Lithos* **2020**, *360–361*, 105449. [[CrossRef](#)]
95. Li, P.; Li, J.K.; Chou, I.M.; Wang, D.H.; Xiong, X. Mineralization Epochs of Granitic Rare-Metal Pegmatite Deposits in the Songpan-Ganzê Orogenic Belt and Their Implications for Orogeny. *Minerals* **2019**, *9*, 280. [[CrossRef](#)]
96. Hao, X.F.; Fu, X.F.; Liang, B.; Yuan, L.P.; Pan, M.; Tang, Y. 2014. Formation ages of granite and X03 pegmatite vein in Jiajika, western Sichuan and their geological significance. *Miner. Depos.* **2014**, *24*, 1199–1208. (In Chinese with English abstract)
97. Dai, H.Z.; Wang, D.H.; Liu, L.J.; Yu, Y.; Dai, J.J. Geochronology and geochemistry of Li (Be)-bearing granitic pegmatites from the Jiajika superlarge Li-polymetallic deposit in Western Sichuan, China. *J. Earth Sci.* **2019**, *30*, 707–727. [[CrossRef](#)]
98. Li, J.K. Mineralizing Mechanism and Continental Geodynamics of Typical Pegmatite Deposits in Western Sichuan, China. Ph.D. Thesis, China University of Geoscience, Beijing, China, 2006. (In Chinese with English abstract)
99. Fei, G.C.; Tian, J.J.; Yang, J.Y.; Gao, J.G.; Tang, W.C.; Li, J.; Gu, C.H. New zircon U-Pb age of the super-large Lijiagou spodumene deposit in Songpan-Garze fold belt, Eastern Tibet: Implications for Early Jurassic rare-metal polymetallic event. *Acta Geol. Sin-Engl.* **2018**, *92*, 1274–1275. [[CrossRef](#)]
100. Chen, X.Z.; Chen, G.C.; Li, R.B.; Zhang, Y.F.; Ji, X.J.; Zhang, X.F. Zircon U-Pb geochronology and trace element characteristics of Wuduoshan granite pegmatite in the eastern part of East Qinling and its geological significance. *Earth Sci.* **2021**. (In Chinese with English abstract) [[CrossRef](#)]

Disclaimer/Publisher's Note: The statements, opinions and data contained in all publications are solely those of the individual author(s) and contributor(s) and not of MDPI and/or the editor(s). MDPI and/or the editor(s) disclaim responsibility for any injury to people or property resulting from any ideas, methods, instructions or products referred to in the content.